
Faculty Work Comprehensive List

2020

Beyond Equilibrium Temperature: How the Atmosphere/Interior Connection Affects the Onset of Methane, Ammonia, and Clouds in Warm Transiting Giant Planets

Jonathan J. Fortney

Channon Visscher

Dordt University, channon.visscher@dordt.edu

Mark S. Marley

Callie E. Hood

Michael R. Line

See next page for additional authors

Follow this and additional works at: https://digitalcollections.dordt.edu/faculty_work

 Part of the [Astrophysics and Astronomy Commons](#)

Recommended Citation

Fortney, J. J., Visscher, C., Marley, M. S., Hood, C. E., Line, M. R., Thorngren, D. P., Freedman, R. S., & Lupu, R. (2020). Beyond Equilibrium Temperature: How the Atmosphere/Interior Connection Affects the Onset of Methane, Ammonia, and Clouds in Warm Transiting Giant Planets. *Astronomical Journal*, 160 (6), 288. <https://doi.org/10.3847/1538-3881/abc5bd>

This Article is brought to you for free and open access by Dordt Digital Collections. It has been accepted for inclusion in Faculty Work Comprehensive List by an authorized administrator of Dordt Digital Collections. For more information, please contact ingrid.mulder@dordt.edu.

Beyond Equilibrium Temperature: How the Atmosphere/Interior Connection Affects the Onset of Methane, Ammonia, and Clouds in Warm Transiting Giant Planets

Abstract

The atmospheric pressure–temperature profiles for transiting giant planets cross a range of chemical transitions. Here we show that the particular shapes of these irradiated profiles for warm giant planets below ~ 1300 K lead to striking differences in the behavior of nonequilibrium chemistry compared to brown dwarfs of similar temperatures. Our particular focus is H₂O, CO, CH₄, CO₂, and NH₃ in Jupiter- and Neptune-class planets. We show that the cooling history of a planet, which depends most significantly on planetary mass and age, can have a dominant effect on abundances in the visible atmosphere, often swamping trends one might expect based on T_{eq} alone. The onset of detectable CH₄ in spectra can be delayed to lower T_{eq} for some planets compared to equilibrium, or pushed to higher T_{eq} . The detectability of NH₃ is typically enhanced compared to equilibrium expectations, which is opposite to the brown dwarf case. We find that both CH₄ and NH₃ can become detectable at around the same T_{eq} (at T_{eq} values that vary with mass and metallicity), whereas these "onset" temperatures are widely spaced for brown dwarfs. We suggest observational strategies to search for atmospheric trends and stress that nonequilibrium chemistry and clouds can serve as probes of atmospheric physics. As examples of atmospheric complexity, we assess three Neptune-class planets, GJ 436b, GJ 3470b, and WASP-107, all around $T_{\text{eq}} = 700$ K. Tidal heating due to eccentricity damping in all three planets heats the deep atmosphere by thousands of degrees and may explain the absence of CH₄ in these cool atmospheres. Atmospheric abundances must be interpreted in the context of physical characteristics of the planet.

Keywords

exoplanet atmospheres

Disciplines

Astrophysics and Astronomy

Authors

Jonathan J. Fortney, Channon Visscher, Mark S. Marley, Callie E. Hood, Michael R. Line, Daniel P. Thorngren, Richard S. Freedman, and Roxana Lupu

Beyond Equilibrium Temperature: How the Atmosphere/Interior Connection Affects the Onset of Methane, Ammonia, and Clouds in Warm Transiting Giant Planets

JONATHAN J. FORTNEY,¹ CHANNON VISSCHER,^{2,3} MARK S. MARLEY,⁴ CALLIE E. HOOD,¹ MICHAEL R. LINE,⁵
DANIEL P. THORNGREN,⁶ RICHARD S. FREEDMAN,^{4,7} AND ROXANA LUPU⁸

¹*Department of Astronomy & Astrophysics, University of California, Santa Cruz, CA 95064, USA*

²*Chemistry & Planetary Sciences, Dordt University, Sioux Center, IA 51250, USA*

³*Space Science Institute, Boulder, CO 80301, USA*

⁴*NASA Ames Research Center Moffett Field, Mountain View, CA 94035, USA*

⁵*School of Earth & Space Exploration, Arizona State University, Tempe AZ 85287, USA*

⁶*Institute for Research on Exoplanets, Université de Montréal, Montréal, Québec, H3T 1J4, Canada*

⁷*SETI Institute, Mountain View, CA 94043, USA*

⁸*BAER Institute, NASA Research Park, Moffett Field, CA 94035, USA*

ABSTRACT

The atmospheric pressure-temperature profiles for transiting giant planets cross a range of chemical transitions. Here we show that the particular shape of these irradiated profiles for warm giant planets below ~ 1300 K lead to striking differences in the behavior of non-equilibrium chemistry compared to brown dwarfs of similar temperatures. Our particular focus is H_2O , CO , CH_4 , CO_2 , and NH_3 in Jupiter- and Neptune-class planets. We show the cooling history of a planet, which depends most significantly on planetary mass and age, can have a dominant effect on abundances in the visible atmosphere, often swamping trends one might expect based on T_{eq} alone. The onset of detectable CH_4 in spectra can be delayed to lower T_{eq} for some planets compared to equilibrium, or pushed to higher T_{eq} . The detectability of NH_3 is typically enhanced compared to equilibrium expectations, which is opposite to the brown dwarf case. We find that both CH_4 and NH_3 can become detectable at around the same T_{eq} (at T_{eq} values that vary with mass and metallicity) whereas these “onset” temperatures are widely spaced for brown dwarfs. We suggest observational strategies to search for atmospheric trends and stress that non-equilibrium chemistry and clouds can serve as probes of atmospheric physics. As examples of atmospheric complexity, we assess three Neptune-class planets GJ 436b, GJ 3470b, and WASP-107, all around $T_{\text{eq}} = 700$ K. Tidal heating due to eccentricity damping in all three planets heats the deep atmosphere by thousands of degrees, and may explain the absence of CH_4 in these cool atmospheres. Atmospheric abundances must be interpreted in the context of physical characteristics of the planet.

1. INTRODUCTION

1.1. Atmospheric Characterization

Even 25 years after the discovery of gas giant exoplanets (Mayor & Queloz 1995) we are still in our infancy in characterizing the atmospheres of these worlds. Over the past two decades, astronomers have made fantastic strides to obtain spectra of exoplanets, but we still have much to do. In the realm of transiting planets, observers have often been hindered by instruments aboard space- and ground-based telescopes that were

never designed for precision time series spectrophotometry. Even as dozens of planets have been seen in transmission spectroscopy (e.g., Sing et al. 2016) and occultation spectroscopy or photometry (e.g., Kreidberg et al. 2014; Garhart et al. 2020) our ability to understand the physics and chemistry of hydrogen-dominated atmospheres has been limited, principally by low signal-to-noise observations and limited wavelength coverage. On the side of the directly imaged planets, telescopes like Keck, VLT, and Gemini have allowed more robust atmospheric spectroscopy, but with a sample size that is so far limited in number (e.g., Konopacky et al. 2013; Macintosh et al. 2015; Gravity Collaboration et al. 2019).

It is with brown dwarfs, now numbering over 1000, with temperatures down to 250 K (Luhman 2014; Ske-

mer et al. 2016) where robust atmospheric characterization has taken place over the past 25 years. The major transitions in atmospheric chemistry and cloud opacity have now been unveiled (Burrows et al. 2001; Kirkpatrick 2005; Helling & Casewell 2014; Marley & Robinson 2015), although major open questions still exist on the role of clouds in shaping the spectra across a range of T_{eff} and surface gravity. However, it should be clear that relying solely on the classic “stellar” fundamental quantities of T_{eff} , $\log g$, and metallicity has already shown its faults for these objects. For instance, time-variability can reach tens of percent, and effects due to rotation rate (Artigau 2018) and viewing angle have now been seen as important to take into account for atmospheric characterization (Vos et al. 2017).

To understand the atmospheres of giant planets we will certainly need a *larger* sample size than the brown dwarfs, for a similar level of understanding, as planets have many additional complicating factors (Marley et al. 2007). For instance, substantial recent work has gone into assessing the *Spitzer* IRAC 3.6/4.5 colors of cooler transiting planets, in order to better assess atmospheric metallicity and the role of CH_4 and CO absorption (Triaud et al. 2015; Kammer et al. 2015; Wallack et al. 2019; Dransfield & Triaud 2020). The wide diversity of colors at a given T_{eq} , much wider than is seen in brown dwarfs at a given T_{eff} (Beatty et al. 2014; Dransfield & Triaud 2020), has been interpreted as needing a large dispersion in atmospheric metallicity and potentially C/O ratio.

Planets present additional complicating physics, such as heating from above, across a range of incident stellar spectral types (Mollière et al. 2015), in addition to a range of UV fluxes. The planets will have diverse day-night contrasts and circulation regimes, likely with very wide range of atmospheric metallicities (Fortney et al. 2013; Kreidberg et al. 2014) and non-solar abundance ratios (Öberg et al. 2011; Madhusudhan et al. 2014; Espinoza et al. 2017). The cooling of the interiors of giant planets – even the cooler giant planets not affected by the hot Jupiter radius anomaly – is also still not fully understood (e.g., Vazan et al. 2015; Berardo & Cumming 2017).

Key science goals of the *James Webb Space Telescope* (*JWST*) and *ARIEL* are to obtain spectra of a wide range of planetary atmospheres (Beichman et al. 2014; Greene et al. 2016; Tinetti et al. 2018). In the realm of transiting giant planets, which have predominantly accreted their atmospheres from the proto-stellar nebula, one aspect of this science will be characterizing planets over a wide range of temperatures, to sample a wide range of transitions in atmospheric chemistry and cloud formation. A significant amount of previous theoretic-

cal and modeling work have gone into trying to predict and understand trends in the atmospheres of these planets, going back to important early works such as Marley et al. (1999) and Sudarsky et al. (2000), supplemented by later works like Fortney et al. (2008), Madhusudhan et al. (2011a), and Mollière et al. (2015). Most of these papers have pointed to planetary equilibrium temperature, T_{eq} , as the dominant physical parameter that determines atmospheric physics and chemistry, somewhat akin to T_{eff} in stars. While there are good reasons to think that this is indeed true, there are equally good reasons to think that T_{eq} is only a starting point, and that other physical parameters can have a crucial effect on determining the atmospheric spectra that we will see.

Of course T_{eq} is only part of the energy budget, and it is well-understood that $T_{\text{eff}}^4 = T_{\text{eq}}^4 + T_{\text{int}}^4$, with T_{int} parameterizing the intrinsic flux from the planetary interior, and T_{eq} from thermal balance with the parent star. In Jupiter, for instance, T_{eq} and T_{int} are similar, with neither dominating the energy budget (Pearl & Conrath 1991; Li et al. 2018). Recently, Thorngren et al. (2019, 2020) pointed out that the radii of “hot” and “warm” Jupiter population can be used to assess the intrinsic flux coming from planetary interiors. Often Jupiter-like values of T_{int} (100 K) had been chosen for convenience, but the inflated radius of a typical hot Jupiter goes hand-in-hand with a hotter interior and much higher T_{int} values (assuming convective interiors).

This work gives us the ability to better assess the depth of the radiative-convective boundary (RCB) in these strongly irradiated planets. A key finding of Thorngren et al. (2019) was the T_{int} values are typically larger (sometimes much larger) than previous expectations, which moves the RCB to lower pressures. A higher T_{int} can remove or weaken cold traps in these atmospheres, which can alter atmospheric abundances and the depth at which clouds form. Much additional work needs to be considered for these hot planets, perhaps much of it in the 3D context, given the large day-night temperature contrasts (Parmentier & Crossfield 2018).

The role of the current paper is to serve as a complement, of sorts, and extension to, the work of Thorngren et al. (2019), but mostly for cooler planets. For planets below $T_{\text{eq}} \sim 1000$ K, a wide range of chemical and cloud transitions should occur (Marley et al. 1999; Sudarsky et al. 2000; Morley et al. 2012). What is not as appreciated, however, is that temperatures in the deeper atmosphere, which are typically not visible, can play as large a role, or even a larger role, in determining atmospheric abundances as the visible atmosphere, which is dominated by absorbed starlight.

The temperatures of the deep atmosphere, while typically not measurable, can be constrained in a variety of ways. Observationally, flux from the deep interior can potentially be seen at wavelengths where the opacity is low (“windows”). This has been constrained for GJ 436b emission photometry (Morley et al. 2017a), and could potentially be done for a small number of other planets (Fortney et al. 2017). Another is cold-trapping gases into condensates via crossing a condensation curve in the deep atmosphere (Burrows et al. 2007; Fortney et al. 2008; Beatty et al. 2019; Thorngren et al. 2019; Sing et al. 2019).

As was done in Thorngren et al. (2019), the planetary radius can be used as a constraint, with assumptions about interior energy transport. Planetary thermal evolution/contraction models aim to understand the cooling of the planetary interior with time (e.g., Fortney et al. 2007; Baraffe et al. 2008). Furthermore, there are planets for which thermal evolution models can be made more uncertain – those that are undergoing tidal eccentricity damping. If this energy is dissipated in the planet’s interior, the temperature of the deep atmosphere can be significantly enhanced compared to simple predictions. Lastly, one can assess the role of disequilibrium chemistry tracers. Recently, Miles et al. (2020) have used observations of disequilibrium CO in cold brown dwarfs to understand atmospheric dynamics and temperature structures. They constrain the rate of atmospheric vertical mixing as a function of T_{eff} , providing strong evidence for a detached radiative zone, below the visible atmospheres, long predicted in these atmospheres (Marley et al. 1996; Burrows et al. 1997). Is it these disequilibrium tracers which we turn to next, in more detail.

1.2. “Hidden” Atmospheric Chemistry

Due to non-equilibrium chemistry via vertical mixing, deep atmosphere temperatures can matter as much as temperatures in the visible atmosphere in determining observable abundances. This well-understood process affects abundances when the mixing timescale for a parcel of gas, t_{mix} , is shorter than the chemical conversion timescale, t_{chem} , for a given chemical reaction. Well-studied reactions are CO to CH₄ and N₂ to NH₃. These timescales can be so long that the gas in the visible atmosphere (at say, 1 mbar) will be representative of pressure-temperature (P - T) conditions at ~ 1 -1000 bar, as we will readily show. The effects of non-equilibrium chemistry on the atmospheric abundances and resulting spectra in giant planet (both solar system and extrasolar) and brown dwarf atmospheres have previously been extensively studied (Fegley & Lodders

1996; Saumon et al. 2003, 2006; Visscher et al. 2010; Visscher & Moses 2011; Moses et al. 2011; Madhusudan et al. 2011a; Venot et al. 2012; Moses et al. 2013; Miguel & Kaltenegger 2014; Zahnle & Marley 2014; Molaverdikhani et al. 2019; Venot et al. 2020; Miles et al. 2020; Molaverdikhani et al. 2020) and here we will not break new ground on the chemistry. Rather, following the carbon and nitrogen chemistry work of Zahnle & Marley (2014), we will point out several novel complexities that arise when applying non-equilibrium chemistry to the quite inhomogeneous exoplanet population. Given the very large uncertainties in vertical mixing speeds, in particular for these irradiated atmospheres that are mostly radiative rather than convective (where mixing length theory could plausibly be used), in addition to uncertainties in thermal evolution models, as well as the currently unknown atmospheric metal-enrichments, we will show that a very wide range of behavior should be expected. For instance, one should not expect a single transition temperature in T_{eq} from CO-dominated to CH₄-dominated atmospheres, an area of active study already with *Hubble* and *Spitzer* (Stevenson et al. 2010; Morley et al. 2017a; Kreidberg et al. 2018; Benneke et al. 2019).

We can first look at an illustrative example of why vertical mixing from different atmospheric depths can strongly affect observed abundances and spectra, by exploring the behavior of CO, CH₄, and H₂O. Figure 1 shows the atmospheric pressure-temperature (P - T) profile for a planet at 0.15 AU from the Sun, with $T_{\text{eq}} = 710$ K. Five models are shown, with decreasing T_{int} , leading to cooler interior adiabats. Underplotted in light gray are curves of constant volume mixing ratio (mole fraction) for CO, to the lower left, following the chemical equilibrium calculations of Visscher et al. (2010) and Visscher (2012). Underplotted in dark gray is the same for CH₄, to the upper right. The dashed thick black curve shows the equal-abundance boundary, where the mixing ratio of CO=CH₄:

$$\log_{10} P \approx 5.05 - 5807.5/T + 0.5[\text{Fe}/\text{H}], \quad (1)$$

for P in bar, T in K, and $[\text{Fe}/\text{H}]$ as the metallicity (Visscher 2012). When we turn to nitrogen chemistry in Section 4.2, we will use the analogous N₂=NH₃ equal abundance curve:

$$\log_{10} P \approx 3.97 - 2721.2/T + 0.5[\text{Fe}/\text{H}] \quad (2)$$

Numbered black dots in Figure 1 have been placed along the profiles. Point 1 is at 1 mbar, a pressure that would be readily probed in transmission spectroscopy. Point 2 is at 700 K, where the local temperature is

Table 1. Guide to Model Parameters

Fig.	T_{eq} (K)	T_{int} (K)	M_J	g (m s $^{-2}$)	m	age (Gyr)
1	710	60, 100, 200, 300, 400	1	25	10×	
4, 23	710	52, 77, 117, 182, 333	0.1, 0.3, 1, 3, 10	5.8, 9.8, 24, 65, 225	10×	3
7, 13	1120 to 180	75	0.3	10	10×	3
9, 15	870, 380, 180	52, 117, 333	0.1, 1, 10	5.8, 24, 225	10×	3
11, 17	710	501, 383, 283, 212, 156, 117, 84	1	13, 16, 19, 21, 23, 24, 26	3×	0.01, 0.03, 0.1, 0.3, 1.0, 3.0, 10.0
19	870, 380	52, 117, 333	0.1, 1, 10	5.8, 24, 225	1, 3, 50×	3

NOTE—In each figure, a range of planetary models is considered explored across different planetary parameters. The metallicity factor m is defined as $m = 10^{[\text{Fe}/\text{H}]}$.

equal to T_{eff} , a good representation of the mean thermal photosphere in emission. Points 1 and 2 are in the CH_4 -dominated region, with point 2 having $\sim 10\times$ more CO. Moving down to point 3, all profiles are now in the CO-dominated regime, where the CH_4 abundance falls off dramatically with temperature. Point 4 is deeper in the atmosphere along the hottest adiabat, in the CO-rich region, with a decrease in CH_4 compared to point 3. Points 5 and 6 are along cooler adiabats, with 5 having abundances quite similar to point 3. Point 6 is quite interesting, in that, while it is in the deep part of the atmosphere, it is clearly within the CH_4 -dominant region, and has the same CH_4 and CO abundances as point 2. This complexity should be contrasted with the profile of a $T_{\text{eff}} = 1000$ K, $\log g = 5$ brown dwarf, plotted in thick orange. For the brown dwarf, as a parcel of gas moves along from high pressure to low, there is a monotonic increase in CH_4 and decrease in CO.

As one would expect, the spectra that use the quenched abundances, brought up to the visible atmosphere from the black points of Figure 1, vary considerably as the abundances of CO and CH_4 vary by orders of magnitude. In addition, the abundance of H_2O changes depending on whether CO is present as well. We demonstrate this for 5 different models shown in Figure 2. For points to the “right” of the CO/ CH_4 equal-abundance curve, like 3, 5, and especially 4, the CO band is much stronger, and CH_4 weaker. The spectra from points 1 and 6 are substantially similar, given their relatively positions in CO/ CH_4 phase space. The lack of monotonic behavior in the mixing ratio (and observability) of CH_4 as a function of the quench pressure was also pointed out for by Molaverdikhani et al. (2019, see their Figure 2), although they did not explore variations in the lower boundary condition, which is our focus here.

Such a wide range of internal adiabats, for a given upper atmosphere, is quite possible due to the differences in cooling histories in giant planets. It is by now widely appreciated that giant planets cool over time, most dra-

matically at young ages, and that more massive planets take longer to cool (Marley et al. 1996; Burrows et al. 1997; Chabrier & Baraffe 2000). For reference, in Figure 3 we plot cooling tracks for planets from $10 M_J$ to $0.1 M_J$ ($32 M_\oplus$) for ages from 10^7 to 10^{10} years, using the models of Fortney et al. (2007) and Thorngren et al. (2016). At an age of 3 Gyr, for instance, T_{int} values of 50 K to 350 K span the population. Such model planets would in reality all have different surface gravities, which would then yield different P - T profile shapes, even at

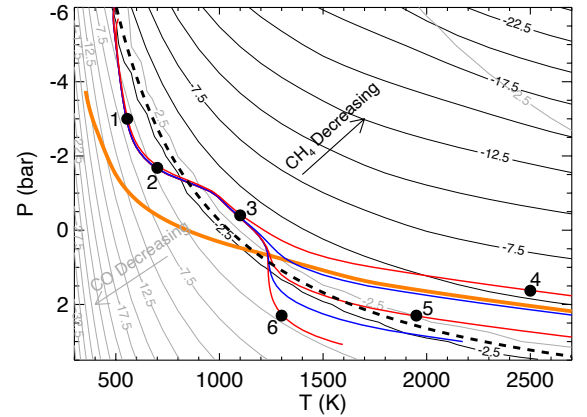


Figure 1. Model pressure-temperature profiles for a $10\times$ solar atmosphere at 0.15 AU from the Sun. The five profiles all have $T_{\text{eq}} = 710$ K and show (alternating red and blue) five values of T_{int} , at 60, 100, 200, 300, and 400 K and a Jupiter-like gravity of 25 m s^{-2} . Also shown in thick orange is a T_{eff} of 1000 K brown dwarf with a gravity of 1000 m s^{-2} . Equal-abundance contours for CH_4 are shown in dark gray, and show the log (base 10) of volume mixing ratios of CH_4 that fall off by many orders of magnitude towards the upper right. Correspondingly, light gray contours show the same for CO, toward the lower left, where CH_4 is the dominant absorber. CO and CH_4 have an equal abundance at the dashed thick black curve. These mixing ratio contours assume equilibrium chemistry. The numbered black dots are called out specifically in the text.

the same orbital separation, as shown in Figure 4. This plot is for the expected surface gravity for the five planet masses (at an age of 3 Gyr) shown in Figure 3.

Taken as a whole, these simple examples serve as motivation to explore a wider range of parameter space

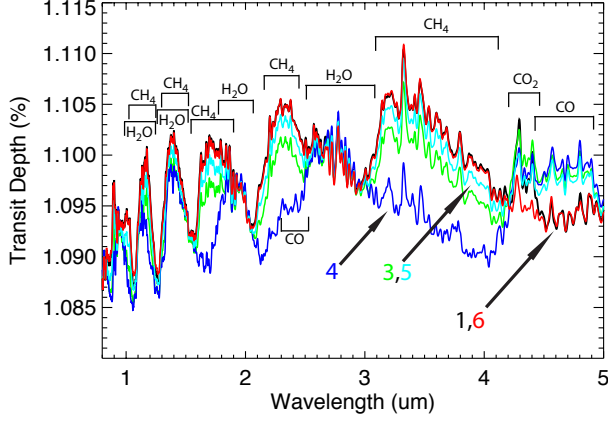


Figure 2. The corresponding transmission spectra for the P - T profiles and chemical abundance points from Figure 1. The main absorption features of H_2O , CO , CH_4 , and CO_2 are labeled. Transmission spectra that use the “quenched” chemical abundances from points 1, 3, 4, 5, and 6 are labeled with arrows. Spectra are normalized to wavelengths where H_2O is the main absorber, to show the relative roles of CO and CH_4 in shaping spectra. The transit models assume $1 R_J$ at a pressure of 1 kbar, a gravity of 25 m s^{-2} , and stellar radius of the Sun.

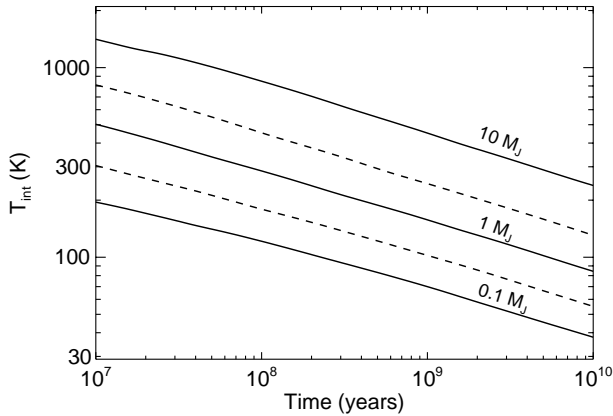


Figure 3. Thermal evolution of giant planets at 0.1 AU from the Sun, after Fortney et al. (2007) and Thorngren et al. (2016). Plotted are the intrinsic effective temperature, T_{int} , for models at 10, 3, 1, 0.3, and $0.1 M_J$ ($32 M_{\oplus}$), from top to bottom. For reference, Jupiter today has $T_{\text{int}} = 99 \text{ K}$. A wide range of T_{int} values are possible at old ages, given a range of planetary masses, and a wide range of T_{int} values are possible at a given mass, over time.

for H/He -dominated atmospheres. The aim then is to show that a range of factors other than equilibrium temperature can have significant impacts, even *dominant* impacts, on atmospheric abundances and spectra. We also explore how non-equilibrium chemistry can serve as a tracer for understanding the deep temperature structure for these atmospheres, at pressures far below where one can probe directly. After describing our methods in a bit more detail, we investigate these factors, first for well-known transiting Neptune-class planets GJ 436b, GJ 3470b, and WASP-107. After that we will explore carbon chemistry more generally, followed by nitrogen chemistry more generally, before our Discussion (with caveats), and Conclusions.

2. MODEL DESCRIPTION

2.1. Atmospheric Structure and Spectra

The model atmosphere methods used here have previously been extensively described in the literature. We compute planet-wide average (“ 4π re-radiation of absorbed stellar flux”) 1D radiative-convective equilibrium models using the model atmosphere code described in the papers of Marley & McKay (1999), Marley et al. (1996), Fortney et al. (2005), Fortney et al. (2008), and the general review of Marley & Robinson (2015). The radiative transfer methods are described in McKay et al. (1989). The model uses 90 layers, typically evenly spaced in log pressure from 1 microbar to 1300 bars.

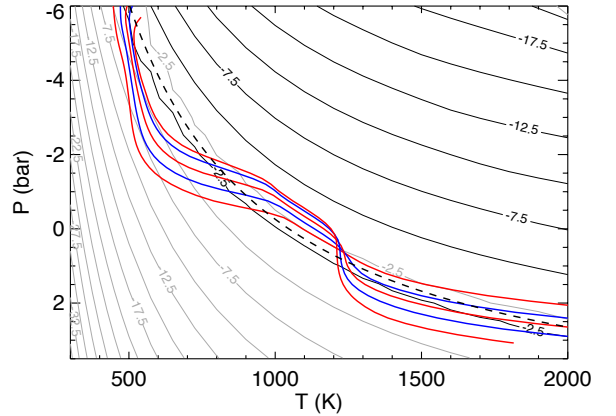


Figure 4. Model pressure-temperature profiles (with $T_{\text{eq}} = 710 \text{ K}$) for a $10\times$ solar atmosphere at 0.15 AU from the Sun, this time based on thermal evolution models. The five profiles (alternating red and blue) show five values of T_{int} , at 52, 77, 117, 182, and 333 K, as respective surface gravities $g = 5.8, 9.8, 24, 65,$ and 225 m s^{-2} . Equal-abundance contours for CH_4 are shown in black, and light gray contours show the same for CO . CO and CH_4 have an equal abundance at the dashed thick black curve. These mixing ratio contours assume equilibrium chemistry.

The equilibrium chemical abundances follow the work of Lodders & Fegley (2002), Visscher et al. (2006, 2010) and Visscher (2012). The opacity database is described in Lupu et al. (2014) and Freedman et al. (2014). Transmission spectra are calculated using the 1D code described in Morley et al. (2017b).

2.2. Interiors and Tidal Heating

As already mentioned, the giant planet thermal evolution models use the methods of Fortney et al. (2007) and Thorngren et al. (2016). These thermal evolution calculations use an extensive grid of 1D non-gray solar-composition radiative-convective atmosphere models, which serve at the upper boundary condition. The interior H/He equation of state is that of Saumon et al. (1995). We make the standard, typical assumption of a fully-convective H/He envelope, and these evolution models also have a $10 M_{\oplus}$ ice/rock core.

Tidal heating, to be investigated in a Section 3, uses the extensive tidal evolution equations derived in Leconte et al. (2010). We determine the tidal heating rate (in energy per second) with equation (13) in this work. We will show that for some planets this tidal heating flux from the interior can be orders of magnitude higher than that calculated from normal secular cooling of the interior.

2.3. Nonequilibrium Chemistry

When treating non-equilibrium chemistry, an important topic in this paper, we make extensive use of the findings of Zahnle & Marley (2014). These authors provide quenching relations that are derived by fitting to the complete chemistry of a full ensemble of 1D kinetic chemistry models. We use the standard “quench pressure” formalism, where we assume chemical equilibrium where the chemical conversion time, t_{chem} , is shorter than the vertical mixing time, t_{mix} . The local values of t_{mix} along a P - T profile use the standard assumption that $t_{\text{mix}} = L^2/K_{zz}$, where L a length scale of interest, here assumed to be the local pressure scale height, H , and K_{zz} is the vertical diffusion coefficient. Other, potentially smaller values of L could be used (Smith 1998; Visscher & Moses 2011), however, as we discuss below, uncertainties in K_{zz} dwarf any uncertainty in L , so, following Zahnle & Marley (2014), we make the simplest choice.

For these strongly irradiated planets, atmospheres can be radiative until depths of tens of bars, even beyond ~ 1 kbar, depending on the the value of T_{int} . The lower the value of T_{int} , the deeper the radiative zone, as shown in Figure 1. While in convective zones mixing length theory can be used as a guide to values of K_{zz} (Gierasch &

Conrath 1985), in radiative regions no such readily usable theory exists, although it is generally expected that radiative regions will have orders of magnitude lower K_{zz} values.

Some 3D circulation model simulations of hot Jupiters have attempted to gauge reasonable K_{zz} values. Parmentier et al. (2013) suggested a fit to models of planet HD 209458b that yielded $K_{zz} = 5 \times 10^8 / \sqrt{P_{\text{bar}}} \text{ cm}^2 \text{ s}^{-1}$. They suggest that cooler planets, like the ones treated here, should have slower vertical wind speeds and smaller values of K_{zz} . More recent work has tried to estimate K_{zz} from first-principles (Zhang & Showman 2018a,b; Menou 2019).

The chemical kinetics literature for irradiated planets shows a range of K_{zz} choices. These include basing values tightly on 3D simulations, but more commonly, choosing a wide-range of constant-with-altitude K_{zz} values, to bracket a reasonable parameter space. It is this bracketing choice that we make here, as we aim to make the point that non-equilibrium chemistry must be important for a wide range of objects. For calculations for particular planets of interest it may be worthwhile to generate K_{zz} predictions from GCM simulations. We return to this point in Section 5. Followup work that couples planetary temperature structures with detailed predictions of K_{zz} profiles (Zhang & Showman 2018a,b; Menou 2019), to predict atmospheric abundances, would be important and fruitful work.

Before exploring a wide range of planets, we first investigate how our models can be used to understand the atmospheric abundances of three (relatively) well-studied Neptune-class transiting planets, which have been the targets of many observations with *Spitzer* and *Hubble*.

3. THE ATMOSPHERES OF THREE NEPTUNE-CLASS PLANETS: GJ 436B, GJ 3470B, WASP-107B

Our first foray into why T_{eq} is not enough will be for the Neptune-class exoplanets, GJ 436b, GJ 3470b, and WASP-107b. These three planets have been the targets of extensive observational campaigns, in particular for GJ 436b, as it was the first transiting Neptune-class planet found (Gillon et al. 2007). The work on emission and transmission observations and their interpretation for this planet is large and difficult to concisely summarize. A recent review can be found in Morley et al. (2017a). The most significant finding, going back to Stevenson et al. (2010), is the suggestion that the planet’s atmosphere is far out of chemical equilibrium, with little CH_4 absorption and a likely high abundance of CO and/or CO_2 . An upper limit on the CH_4 abundance is published in Moses et al. (2013).

More recently, Benneke et al. (2019) found that a joint retrieval of the emission and transmission data for GJ 3470b points to a somewhat similar conclusion, with a lack of CH_4 seen. And a transmission spectrum of WASP-107b by Kreidberg et al. (2018) finds no sign of CH_4 in the near infrared. For both planets, these papers include CH_4 abundance upper limits.

While these three planets have masses and radii that differ by a factor of around 2, they share some interesting similarities. Perhaps most strikingly, they have T_{eq} values that all within ~ 100 K of each other. This *may* suggest that the planets could have similar atmospheric properties. Another, perhaps surprisingly fact, is that all three planets are on eccentric orbits. Most important to our current discussion is that we find all three planets are currently undergoing significant eccentricity damping today.

Figure 5 shows model P - T profiles for all three planets, with GJ 436b in blue, GJ 3470b in red, and WASP-107b in orange. For simplicity, all are at $100\times$ solar, a value similar to the carbon abundance inferred for Uranus and Neptune. We note that retrieval work for GJ 436b (Morley et al. 2017a) suggests a metallicity higher than this value, retrievals for GJ 3470b suggest a metallicity lower than this (Benneke et al. 2019), and preliminary structure models (that did not take into account tidal heating) for WASP-107b also suggested a lower metallicity (Kreidberg et al. 2018). Our aim here is not to find best fits for the spectra of each planet, but to suggest that tidal heating in the interior plays a large role in altering atmospheric abundances. We therefore feel that a simple, but plausible metallicity, can serve as an illustrative example.

A cursory glance shows that all 3 planets reside in a *remarkably similar* P - T space. For these planets 4 adiabats are shown. First we will examine the coolest adiabats (lowest specific entropy), which are for models with no tidal heating ($T_{\text{int}} = 60\text{K}$), and then 3 warmer adiabats that assume $\log Q = 6, 5$, and 4 , from colder to hotter, as a lower Q means more tidal heating (Leconte et al. 2010). Tidal heating for these planets has a dramatic effect, warming the interior by hundreds to *thousands* of K at a given pressure.

All three planets have three sets of solid dots on their profiles that show the quench pressure level for $\log K_{zz} = 4, 8$, and $12 \text{ cm}^2 \text{ s}^{-1}$. For the quench pressure for $\log K_{zz} = 4$, very sluggish mixing, tidal heating has a modest impact in shifting the expected chemical abundances

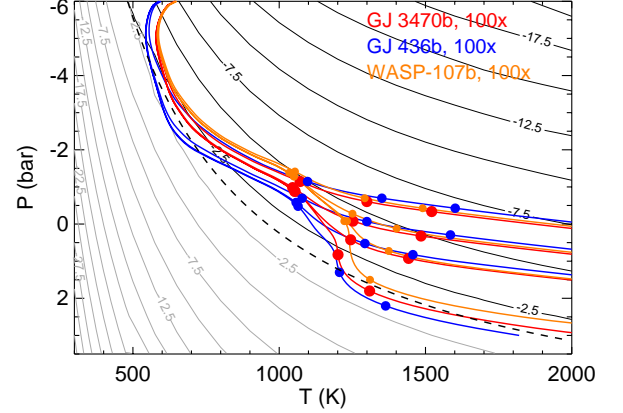


Figure 5. Atmospheric P - T profiles for planets GJ 436b, GJ 3470b, and WASP-107b all at $100\times$ solar abundances. The light and dark gray equal-abundance curves are similar to those in Figure 1, although here we plot $100\times$ solar. For each planet, 4 interior adiabats are shown, for the case of no tidal heating (coolest), and $Q = 10^6, 10^5$ and 10^4 , from cooler to warmer. The sets of solid dots show the quench pressure for $\log K_{zz} = 4, 8, 12$, where larger K_{zz} values probe deeper.

to CO-richer and CH_4 -poorer territory, compared to, say, equilibrium chemistry at 1 mbar. However, for the depths probed at $\log K_{zz} = 8$ and 12 , the atmosphere models are significantly warmer, and draw from a region of much higher CO and lower CH_4 if heating is present. We can explore and quantify this effect for a subset of models, which are shown in Figure 6, where each planet has its own panel. Abundances at 1 mbar are plotted for equilibrium chemistry and $\log K_{zz} = 4, 8$, and 12 . Thin lines are for no tidal heating, while thick lines include tidal heating, with $Q = 10^4$ – a reasonable estimate for Neptune (Zhang & Hamilton 2008) – for GJ 3470b and WASP-107b, and $Q = 10^5$ for GJ 436b, based on a fit to the planet’s thermal emission spectrum (Morley et al. 2017a). At our assumed $100\times$ abundances with equilibrium chemistry, for all three planets CH_4 would be expected to be abundant, and even the dominant carbon carrier in GJ 436b and WASP-107b. The retrieved 1σ CH_4 upper limits, from free retrievals from all three atmospheres (Moses et al. 2013; Kreidberg et al. 2018; Benneke et al. 2019), are shown as dashed black lines.

There are two main effects to be seen in Figure 6. First in the large change in abundances for CH_4 – falling off dramatically, and CO – increasing, but more modestly, just in going from equilibrium chemistry to $\log K_{zz} = 4$. Another striking effect is the divergence in the behavior of the CH_4 abundance at $\log K_{zz} = 8$ and 12 , between the no tidal heating model (thin lines) and the model with tidal heating. Based on the P - T profiles in Figure 5 we

¹ $\log K_{zz} \sim 10.5$ is the maximum allowed from mixing length theory, for GJ 3470b and WASP-107b, for the hottest interior profiles shown, per equation 4 from Zahnle & Marley (2014).

can see that no-heating models bring up CH_4 -rich gas, while the tidal heating models bring up CH_4 -poor gas. This is a dramatic effect in all three planets. Large K_{zz} values, driven by strong convection caused by ongoing tidal dissipation, can drive the CH_4 abundance to low values, in the range constrained by observations to date.

This strongly suggests that nonequilibrium chemistry and tidal heating conspire to drive the atmospheric abundances far from simple expectations. We should of course be a bit wary about treating the three planets as *carbon copies* however. With no theory to guide the strength of tidal heating, Q for the planets could be quite different for all three. The expected mass fraction of H/He in WASP-107b is far larger than for GJ 3470b, for instance. Similarly, with little theory to guide vertical mixing strength, this could also be quite different among the planets, as they have quite different surface gravities. Additionally, they have been modeled with relatively simple chemical abundances ($100\times$ solar, with a solar C/O ratio), and the actual planets could readily have more complex, and different, base elemental abundances. Of note, the planet WASP-80b, about $100\text{--}150\text{ K}$ warmer than this trio, but on a circular orbit (Triaud et al. 2015), has a *Spitzer* IRAC $3.6/4.5\text{ }\mu\text{m}$ ratio in thermal emission that is similar to early T-dwarfs. Triaud et al. (2015) suggest this IRAC color could potentially be due to some CH_4 absorption in the planet’s atmosphere, which seems quite viable, as we describe in the next section.

As Morley et al. (2017a) suggested for GJ 436b, a direct sign of tidal heating would be a high thermal flux from the planet’s interior, which could be observed via a secondary eclipse spectrum or thermal emission phase curve. Future observations with *JWST*, including those where tidal heating are not at play, may allow for a coupled understanding of atmospheric abundances, temperature structure at a variety of depths, vertical mixing speed, and tidal heating. These three planets, all in a similar $P\text{--}T$ space, motivate a wider investigation.

4. THE PHASE SPACE OF CHEMICAL TRANSITIONS

In the face of vertical mixing altering chemical abundances, mixing ratios in the visible atmosphere are tied to atmospheric temperatures at depth, as described in the previous section. This complicates the goal of deriving a straightforward understanding of chemical transitions. We aim to show that, even at a given metallicity and K_{zz} , this transition will depend on the cooling history (hence, mass and age) of any planet. We refer back to Figure 3 which showed models of the thermal evolution of giant planets. These model planets are all at

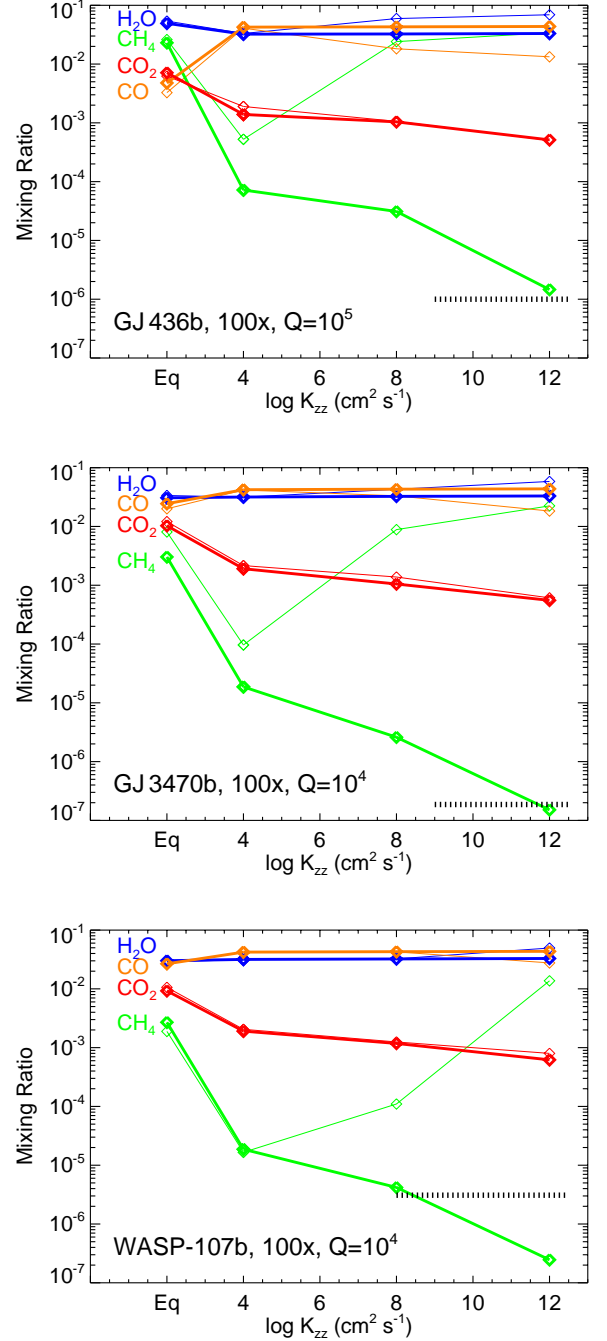


Figure 6. Top: Chemical abundances at 1 mbar for 3 models of GJ 436b. H_2O is blue, CO is orange, CO_2 is red, and CH_4 is green. Plotted are abundances for equilibrium chemistry, and $\log K_{zz} = 4, 8$, and 12 . Thin lines show no tidal heating, while thick lines use $Q = 10^5$. With tidal heating, the higher the K_{zz} , the higher the CO/CH_4 ratio. The dashed black line shows the CH_4 mixing ratio upper limit. Middle: A very similar plot for GJ 3470b, again showing how nonequilibrium chemistry and tidal heating enhance the CO/CH_4 ratio, but with $Q = 10^4$. Bottom: Another similar plot for WASP-107b, with $Q = 10^4$. Tidal heating and high K_{zz} can plausibly explain all observations.

0.1 AU from the Sun, but these cooling tracks would be correct, to within several K, at closer or farther orbital distance (Fortney et al. 2007). Therefore, we can investigate, at a fixed value of T_{int} , how changing incident flux (hence, T_{eq}) does or does not lead to changes in chemical abundances in the visible atmosphere. We first explore carbon chemistry.

4.1. CO-CH₄ Transitions

In Section 3 we examined the CO-CH₄ boundary for specific tidally-heated Neptune-class planets. Objects with tidal heating are special cases, but certainly will be common enough that they cannot simply be ignored, when looking at general trends. But here we can examine the general trends in the absence of tidal heating, for a range of planet masses and ages. As we will see, the range of cooling histories, and lack of clarity with how vertical mixing will change with planet mass, can lead to important complexities.

4.1.1. Effects of T_{eq} and Vertical Mixing

We first examine the general case of a Saturn-like exoplanet as a function of distance from a Sunlike star. Here we have chosen a $10\times$ solar atmosphere, surface gravity of 10 m s^{-2} , and $T_{\text{int}} = 75 \text{ K}$, representative of a several gigayear-old Saturn-mass exoplanet. We choose this as our “base planet” since these kinds of giant planets would be excellent targets for atmospheric characterization via transmission. Atmospheric P - T profiles are shown in Figure 7, for planets from 0.06 AU to 2 AU. The three sets of black dots show quench pressures corresponding to $\log K_{zz}$ values of 4, 8, and 11. Most importantly, at lower pressures, the atmospheres diverge quite widely, owing to the factor of ~ 1100 difference in incident flux across these models.

As one looks deeper it is apparent that profiles modestly converge as the pressure increases, followed by a dramatic “squeezing together” as the planets fall on nearly identical adiabats. This is a generic behavior for g/T_{int} pairs, and one could make a plot like this for any Jupiter-like planet, super-Jupiter, or sub-Saturn. Why this behavior occurs requires some discussion. To our knowledge this effect was first noted in Figure 3 of Fortney et al. (2007), who described the effects of these “bunched up” deep profiles on the mass-radius relation for warm transiting giant planets, but they did not identify a cause for the similarity of the deep temperatures.

A study of the gray analytic temperature profiles of Guillot (2010) suggests, via their Equation (29), a relation between the temperature (T) and optical depth τ that is a function of only three quantities: the irradiation temperature (which is directly related to T_{eq}), T_{int} , and γ , the ratio of the visible to thermal opacities. If γ is

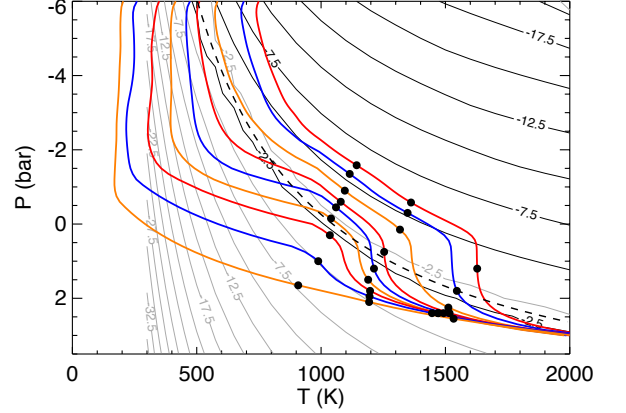


Figure 7. Atmospheric P - T profiles for old, Saturn-like planets ($T_{\text{int}} = 75 \text{ K}$, $g = 10 \text{ m s}^{-2}$, assuming $10\times$ metallicity). The models are a 9 incident flux levels, at 0.06, 0.07, 0.1, 0.15, 0.2, 0.3, 0.5, 1, 2 AU from the Sun. Three sets of black dots show the depth of vertical mixing with $\log K_{zz}$ of 4, 8, and $11 \text{ cm}^2 \text{ s}^{-1}$. At higher pressures, note that the spread between all profiles is lessened, both in temperature, and in reference to the CH₄ (black) and CO (grey) abundance curves.)

relatively constant, and at a given T_{int} value, decreasing T_{eq} cools the entire atmosphere at every τ , including the deep region that here transitions to an adiabat. However, if γ were to dramatically decrease with decreasing T_{eq} , the deep $T - \tau$ profile (analogous to our deep T - P profile) could remain nearly constant at depth with an upper atmosphere that was colder with decreasing T_{eq} . Indeed, Figure 5 of Freedman et al. (2014) shows a factor ~ 60 falloff in γ from ~ 1400 - 700 K , due to the loss of alkali metals Na and K from the vapor phase, with γ relatively constant at hotter and colder temperatures. This 700 - 1400 K temperature range corresponds reasonably well to what is seen in our Figure 7 and “middle region” of Figure 3 of Fortney et al. (2007). Therefore, we suggest that this change in visible opacity is the dominant physical effect the keeps the deep atmosphere temperatures relatively constant across this T_{eq} range. However, additional work on this point is surely needed.

Of particular interest is that the coldest profiles are mostly in the CH₄-dominant region at lower pressures, but along the atmospheric adiabat, as one reaches hotter layers, one finds gradually more CO. This is the “typical” case for brown dwarfs (Saumon et al. 2003; Phillips et al. 2020) and for Jupiter as well (Prinn & Barshay 1977; Lodders & Fegley 2002). However, for the hottest models, this typical trend is reversed, and when one probes quite deeply, one reaches more CH₄-rich gas, in particular at $P > 1 \text{ bar}$, where the isothermal regions are reached.

We can examine how atmospheric abundances are affected by making plots of volume mixing ratio as a function of planetary T_{eq} . Such a plot is shown in Figure 8, and includes all the profiles shown in Figure 7. The mixing ratios at 1 mbar for H_2O , CO , and CH_4 are plotted, for equilibrium chemistry and for $\log K_{zz}$ of 4 and 8. In the equilibrium chemistry case (dashed curves), the changeover from CO -dominant to CH_4 dominant is at about $T_{\text{eq}} = 850$ K. As one goes cooler, this also leads to an increase in the H_2O abundance, as oxygen is liberated from CO (and CO_2).

If we include quite sluggish vertical mixing, with $\log K_{zz} = 4$ (thin solid line), this boundary shifts dramatically left, to a much lower T_{eq} value of only 475 K. The slopes of the CH_4 and CO curves, vs. T_{eq} , are both quite shallow compared to the equilibrium chemistry case and one might readily expect both molecules to be seen from ~ 800 to 200 K. Of course how “detectable” a molecule is depends strongly on the wavelength being investigated, the spectral resolution, and the impact on other opacity sources, like clouds. Given the non-detections of CH_4 with *HST* at mixing ratios of $\sim 10^{-6}$ in the Neptune-class planets (See Section 3), here we suggest $\sim 10^{-5.5}$. However, the 3.3 and 7.8 μm bands of CH_4 and 4.5 μm band of CO are strong and could likely yield detections at lower mixing ratios, in particular at high spectral resolution.

Interestingly, a look back to Figure 7 might suggest that $\log K_{zz} = 8$ case might be a bit less extreme in altering abundances, even though we are mixing up from even hotter layers. The modest pinching together of the P - T profiles yields a behavior in Figure 8 (solid line) that is intermediate between the two previous behaviors, with a crossover T_{eq} of 680 K. Both CO and CH_4 may be seen from $T_{\text{eq}} \sim 900$ to 400 K. The upshot here is that the value of K_{zz} in these atmospheres, and its depth dependence, which is currently unknown, will have a significant effect on the atmospheric abundances as a function of T_{eq} , and a wide range of behavior is expected. As discussed later, given that K_{zz} is unlikely to be constant with altitude, more realistic mixing further complicates this picture.

4.1.2. Effects of Planet Mass at a Given Age

In the previous section we examined one particular planet, a Saturn-like object at different distances from the Sun. However, we have already discussed in some detail in the Introduction that planets of different masses are expected to have quite different cooling histories (Figure 3).

We can begin to address the question of planet mass with three disparate planet examples, with planets of

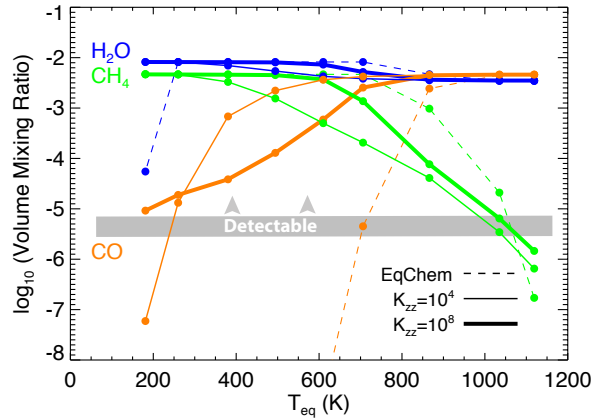


Figure 8. The 9 P - T profiles from Figure 7 are plotted at 9 T_{eq} values across the x-axis, with chemical abundances along the y-axis. “EqChem” gives the chemical equilibrium abundances at 1 mbar (dashed), while $\log K_{zz} = 4$ and 8 are shown as thin solid and thick solid, respectively. In equilibrium, at $T_{\text{eq}} < 800$ K, the CO mixing ratio falls off precipitously, while for $\log K_{zz} = 4$ this falloff is delayed until ~ 500 K cooler. At $\log K_{zz} = 8$ the weakening of CO is also delayed and the change in CO abundance with T_{eq} is much “shallower.” The corresponding increases in CH_4 abundance with lower T_{eq} is again “shallower” for non-equilibrium chemistry. The loss of H_2O in the coolest (equilibrium) model is due to loss of water vapor into water clouds.

10 M_J (a super-Jupiter), 1 M_J and 0.1 M_J (32 M_{\oplus} , a super-Neptune). For now we limit ourselves to the same $10\times$ atmospheric metallicity, so as to not change too many parameters at once. Similar to Figure 7 above, we have computed a range of atmospheric P - T profiles for these 3 planets, at different distances from the Sun, assuming an age of 3 Gyr and the T_{int} values from Figure 3. These profiles are shown in Figure 9. For clarity, profiles are only shown at three distances, 0.1, 0.5, and 2 AU. Along each profile, colored dots, from lower to higher pressure, show $\log K_{zz}$ of 4, 8, and 11, respectively. The more massive the planet, the higher the surface gravity, and the higher pressure at a given temperature, in the outer atmosphere. This, however, is reversed in the deep atmosphere and interior as the higher mass planets take longer to cool, so they have a higher T_{int} (333 K, 117 K, and 52 K, respectively for the 10, 1, 0.1 M_J models) and “hotter” (higher specific entropy) interior adiabat. The much larger scale heights for the low gravity models means greater physical distances for mixing, thus longer mixing times for a fixed K_{zz} , and hence, lower quench pressures.

What we are particularly interested in here is how the role of surface gravity and cooling history work to dramatically change the ratio of CO/CH_4 in these at-

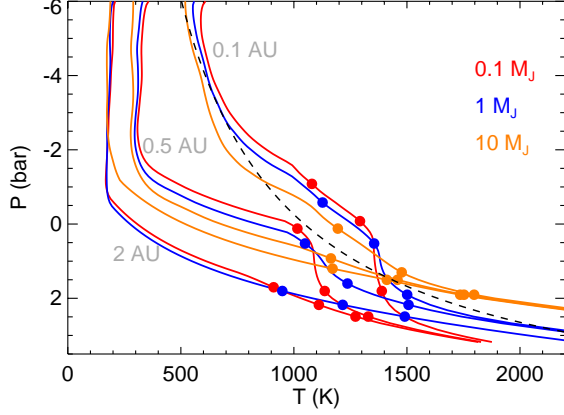


Figure 9. Atmospheric P - T profiles for 3-Gyr-old planets at 0.1 (red), 1 (blue), and 10 (orange) M_J , at $10\times$ solar. The CO/CH_4 equal-abundance curve is in dashed black. The models are at 0.1, 0.5, and 2 AU from the Sun. The color-coded dots show the quench pressure for $\log K_{zz} = 4, 8$, and 11. Higher gravity models have higher pressure photospheres, but also have hotter interiors, which causes significant crossing of profiles. The much larger scale heights for the low gravity models means greater physical distances for mixing, and hence, lower quench pressures.

mospheres. We address this scenario in Figure 10. This abundance ratio is plotted vs. planetary T_{eq} and we will first examine the abundances for equilibrium chemistry at 1 mbar. The “transition” T_{eq} value is 950 K at 10 M_J , and 850 K at 1 and 0.1 M_J . With sluggish vertical mixing ($\log K_{zz} = 4$), the story becomes more complex, however. The 10 M_J planet has a relatively hot interior adiabat, which is essentially the same for all values of T_{eq} , as seen in orange in Figure 9. For such a large value of T_{int} , the smaller values of T_{eq} becomes essentially irrelevant. For the lower mass planets, the transition T_{eq} is much lower than in the equilibrium case, reaching 500 K. For more vigorous mixing ($\log K_{zz} = 8$), more CH_4 -rich gas is brought up, leading to a *hotter* transition temperature, at 700 K.

4.1.3. Effects of Planet Age at a Given Mass

Up until this point, we have examined “old” planetary systems that to date make up the vast majority of the transiting population. However, studying younger transiting planets to better understanding evolutionary histories is extremely important. First, this would yield connections to the directly imaged self-luminous planets, which are predominantly young (Bowler 2016). Second, understanding atmospheric abundances as a function of planet age would give us new insight into planetary thermal evolution. Third, since parent stars are much more

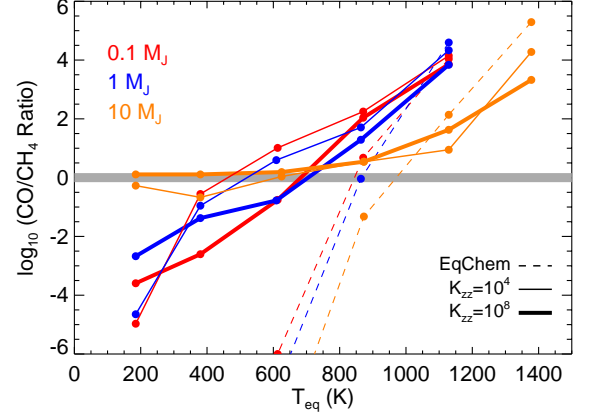


Figure 10. The log of the CO/CH_4 ratio for 5 values of T_{eq} for 0.1, 1, and 10 M_J model planets, where a subset of the profiles are shown in Figure 9. In equilibrium (at 1 mbar), the transition T_{eq} for $\text{CO}/\text{CH}_4 = 1$ ($\log = 0$, shaded grey) is at $\sim 800, 950$, and 1150 K, from low mass to high mass. As expected, vertical mixing lessens the slopes of these curves, and pushes the transition T_{eq} lower for the 0.1 and 1 M_J models. The 10 M_J model quenches from CH_4 -richer gas, at high T_{eq} , which yields the opposite behavior. For all three model planets, CO and CH_4 exist together in detectable amounts for a wide swath of T_{eq} values.

active when they are young, high XUV fluxes for young systems could drive quite interesting photochemistry.

In the absence of tidal heating giant planet interiors inexorably cool as they age, meaning cooler interior adiabats and lower T_{int} values. In the face of vertical mixing, we should expect atmospheric abundances to change then as well. We examine the effect on a range of P - T profiles for a Jupiter-like example (1 M_J , $3\times$ solar) at 0.15 AU in Figure 11. The values of T_{int} are taken from every half-dex in planetary thermal evolution from an age of 10 Myr to 10 Gyr, yielding 7 models from T_{int} of 501 K to 84 K. For moderately irradiated planets like these, the cooling of the interior has little effect on the upper atmosphere (Sudarsky et al. 2003), but we should expect quite different atmospheric abundances when including vertical mixing. The 3 sets of black dots in Figure 11 show $\log K_{zz}$ of 4, 8, and 11.

In Figure 12 we examine the corresponding chemical abundances for equilibrium and the 3 values of vertical mixing strength, as a function of planetary age. In equilibrium at 1 mbar, the atmosphere is CH_4 dominated, and the CO mixing ratio is nearly off the bottom of the plot. However, even very modest vertical mixing ($\log K_{zz} = 4$, thin lines) changes the picture. The atmosphere becomes modestly CO-dominated, and we lose essentially all sensitivity to the deeper atmosphere of the planet – the abundances depend very little on

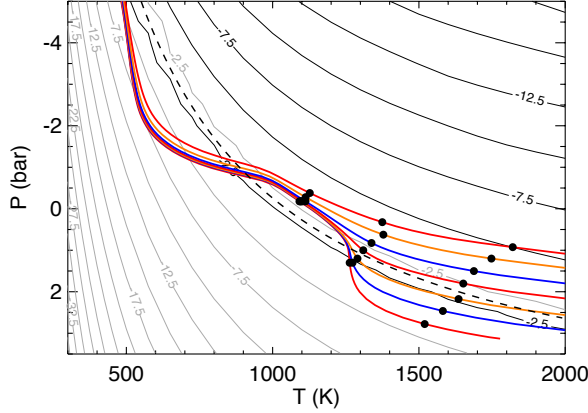


Figure 11. Atmospheric P - T profiles for a $1 M_J$ planet at 0.15 AU from the Sun, assuming $3\times$ solar metallicity. Seven ages, every half dex from 10 Myr to 10 Gyr, with seven values of T_{int} (501, 383, 283, 212, 156, 117, 84 K) are shown. The planetary surface gravity also changes among the models. The three collections of black dots show quench pressures for $\log K_{zz} = 4, 8$, and 11 . At depth, hotter profiles are clearly CO rich, while cooler profiles are CH_4 -rich.

T_{int} . However with more vigorous vertical mixing, we see a picture emerge that has much in common with our understanding of non-equilibrium chemistry in brown dwarfs. Higher T_{int} values and hotter interiors lead to more CO and less CH_4 . The plot shows a changeover from CO-dominated to CH_4 -dominated at ~ 200 Myr, at a T_{int} value of ~ 250 K. Again, this is generic behavior, as more massive objects would transition later in life (but at higher T_{int} values given their higher pressure photospheres and the positions of the CO and CH_4 iso-composition curves), and less massive objects earlier (but at higher T_{int} values, given their lower pressure photospheres). While we expect building up a large sample of atmospheric spectra size a function of planetary age will be a challenge, it will be rewarding to have a statistical sample to compared to the typical several-Gyr-old systems. This could yield important insights into planetary cooling history and the vigor of vertical mixing with age.

4.2. N_2 - NH_3 Transitions

Nitrogen chemistry is predominantly a balance between N_2 and NH_3 , and has been explored and validated in the brown dwarf context (e.g., Saumon et al. 2000, 2003; Cushing et al. 2006; Hubeny & Burrows 2007; Zahnle & Marley 2014). N_2 is favored at high temperatures (and low pressures) while NH_3 is favored at low temperatures (and high pressures). The transition from N_2 to NH_3 at cooler temperatures has a similar character to that of CO converting to CH_4 , but it occurs at lower

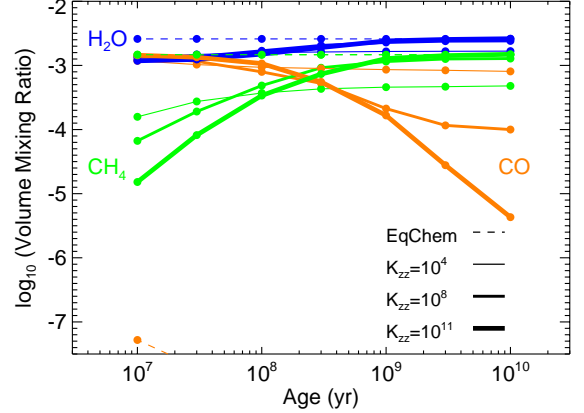


Figure 12. Atmospheric abundances at 1 mbar as function of planetary age, for the P - T profiles shown in Figure 11. In equilibrium (dashed), the cooling of the planet's interior has *no effect* on the atmospheric abundances, as the temperatures of the upper atmosphere are essentially constant, and the atmosphere could be CH_4 -rich and quite CO-poor. Modest vertical mixing ($\log K_{zz}=4$) yields a much higher CO/ CH_4 ratio, but abundances that again are essentially constant with time. More vigorous mixing, from higher quench pressures, samples a much wider range of CO and CH_4 abundances. As the interior cools off the atmosphere transitions from CO-rich to CH_4 rich.

temperatures. Understanding non-equilibrium nitrogen chemistry in brown dwarfs has typically been hampered by two constraints. The first is that N_2 , with no permanent dipole, has no infrared absorption features, unlike CO. The second is that NH_3 iso-composition curves have slopes that lie nearly along interior H/He adiabats, meaning that one typically cannot assess a given atmosphere's quench pressure, as all pressures along the adiabat correspond to nearly the same NH_3 mixing ratio.

However, in some sense irradiated planets have the advantage of having relatively more isothermal P - T profiles, which can remain non-adiabatic to pressure of ~ 1 kbar. And, *if* these predominantly radiative atmospheres have K_{zz} values less than their mostly convective brown dwarf cousins, then it may be these more isothermal radiative parts of the atmosphere where one may quench the chemistry. We can examine this with the same Saturn-like P - T profiles we first examined in Figure 7. These profiles, but now with quench pressures for N_2 - NH_3 chemistry (Zahnle & Marley 2014), are shown in Figure 13.

Underplotted in black are curves of constant NH_3 abundance, falling off at higher temperature and lower pressure. Underplotted in grey are curves of constant N_2 abundance, falling off at lower temperature and higher pressure. A detailed look at Figure 13, compared to

Figure 7, shows that the NH_3 iso-composition curves are more “spread out” than similar curves for CH_4 , suggesting a more gradual change in nitrogen chemistry, with temperature, than for carbon. As the chemical conversion times for $\text{N}_2 \rightarrow \text{NH}_3$ are longer than for $\text{CO} \rightarrow \text{CH}_4$, the corresponding quench pressures for $\log K_{zz} = 4, 8$, and $11 \text{ cm}^2 \text{ s}^{-1}$ are at somewhat higher pressures. While for vigorous mixing ($\log K_{zz} = 11$), all profiles converge to the same quench pressure (and hence changes in T_{eq} across this range would yield no change in the NH_3 abundance, there are a broad ranges of N_2 and NH_3 mixing ratios for the $\log K_{zz} = 4$ and $K_{zz} = 8$ cases.

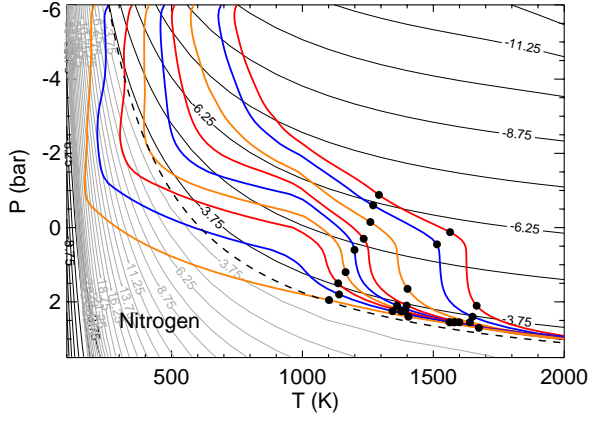


Figure 13. Atmospheric P - T profiles for old, Saturn-like planets ($T_{\text{int}} = 75 \text{ K}$, $g = 10 \text{ m s}^{-2}$, assuming $10\times$ metallicity). The models are a 9 incident flux levels, at 0.06, 0.07, 0.1, 0.15, 0.2, 0.3, 0.5, 1, 2 AU from the Sun. Three sets of black dots show the nitrogen quench pressure for $\log K_{zz}$ of 4, 8, and $11 \text{ cm}^2 \text{ s}^{-1}$. At higher pressures, note that the spread between all profiles is lessened, both in temperature, and in reference to the NH_3 (black) and N_2 (grey) abundance curves.

Figure 14 shows the mixing ratios of N_2 and NH_3 as a function of planetary T_{eq} . Equilibrium chemistry (at 1 mbar) shows a crossover from N_2 -dominant to NH_3 dominant at around 475 K. However, even sluggish vertical mixing keeps all of these atmospheres N_2 dominant, while also increasing the NH_3 mixing ratio for all T_{eq} values $> 600 \text{ K}$. More vigorous mixing ($\log K_{zz} = 8$) further flattens the slope of the NH_3 curve, leading to relatively abundant NH_3 at essentially all T_{eq} values, as expected from the grouping of most of the $\log K_{zz} = 8$ black dots in Figure 13. Across the entire phase space, the NH_3 mixing ratios are similar to those of CH_4 (see Figure 8), and are actually even *higher* for NH_3 than for CH_4 for the higher T_{eq} values. This suggests that onset of detectable CH_4 in these planets should be accompanied by NH_3 as well – one will not need to wait for particularly

cold temperatures, compared to the brown dwarfs. For those interested in determining the relative abundances of C, N, and O, to compare to Jupiter’s values (Wong et al. 2004), we note that in these models NH_3 never becomes the dominant nitrogen carrier compared to N_2 , such that the nitrogen abundance determined from NH_3 would only be a lower limit.

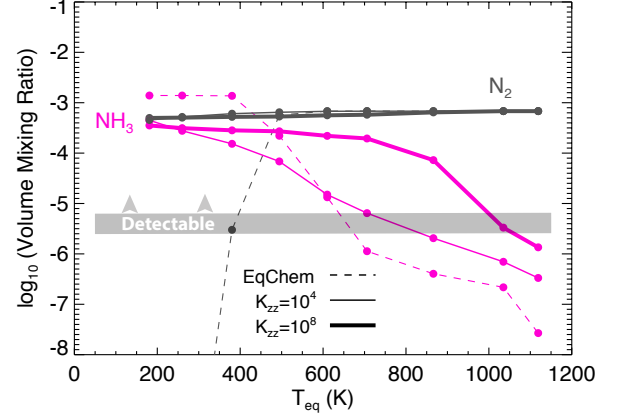


Figure 14. The 9 P - T profiles from Figure 13 are plotted at 9 T_{eq} values across the x-axis, with chemical abundances along the y-axis. “EqChem” gives the nitrogen chemical equilibrium abundances at 1 mbar (dashed), while $\log K_{zz} = 4$ and 8 are shown as thin solid and thick solid, respectively. In equilibrium, at $T_{\text{eq}} \sim 480 \text{ K}$, the N_2 and NH_3 mixing ratios crossover, while for all models with vertical mixing, this crossover does not happen. The more vigorous the vertical mixing, generally, the higher NH_3 mixing ratio, except for the coldest models.

4.2.1. Effects of Planet Mass at a Given Age

Previously, in Section 4.1.2 and Figures 9 and 10 we investigated the role that surface gravity and cooling history have for the planets. Here, we examine the same profiles, but for nitrogen chemistry. Figure 15 shows these sample P - T profiles for the 0.1, 1.0, and $10 M_J$ planets, with $\log K_{zz} = 4, 8$, and 11. Compared to the carbon example from Figure 9, the quench pressures are higher. For the high gravity ($10 M_J$) planet in particular, the quench pressure is within the deep atmosphere adiabat for $\log K_{zz} = 8$ and 11, and near it for $\log K_{zz} = 4$. We might expect that the NH_3 abundance will change little with K_{zz} , similar to a brown dwarf case (Zahnle & Marley 2014). The deeper one probes, the closer one comes to these adiabats, which lie nearly parallel to curves of constant NH_3 abundance. Instead, the NH_3 mixing ratio is in some sense a probe of the current specific entropy of the adiabat, which could prove useful in constraining thermal evolution models.

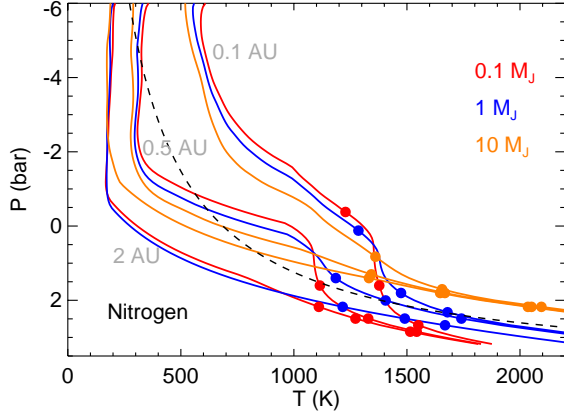


Figure 15. Atmospheric P - T profiles for 3-Gyr-old planets at 0.1 (red), 1 (blue), and 10 (orange) M_J , at $10\times$ solar. The N_2/NH_3 equal-abundance curve is shown in black. The models are at 0.1, 0.5, and 2 AU from the Sun. The color-coded dots show the nitrogen quench pressure for $\log K_{zz} = 4, 8$, and 11. Higher gravity models have higher pressure photospheres, but also have hotter interiors, which causes significant crossing of profiles. The much larger scale heights for the low gravity models means greater physical distances for mixing, and hence, lower quench pressures. Compared to Figure 9, the nitrogen chemistry quench pressures are at higher pressures than for carbon chemistry. For high gravity and/or cool models, the quench pressure is near or within the deep atmosphere adiabat.

We can examine the N_2/NH_3 ratio as a function of T_{eq} for these three planets in Figure 16. The crossover T_{eq} for nitrogen chemistry, in equilibrium, would be ~ 550 K at 10 M_J , 500 K at 1 M_J , and 475 K at 0.1 M_J . However, even modest vertical mixing dramatically changes this picture. As the T_{eq} decreases, the quench pressure falls near or into the deep atmosphere adiabat, even at low gravity. On Figure 15 this manifests as the N_2/NH_3 ratio asymptoting to values that depend solely on the specific entropy of the adiabat, as one might have expected for the specific cases investigated for the Saturn-like planet in Figure 14. Much like the brown dwarfs, at cool temperatures (and especially at high surface gravity) planets here are insensitive to K_{zz} .

4.2.2. Effects of Planet Age at a Given Mass

Previously in Section 4.1.3 and Figures 11 and 12 we found that planet age, and hence, the cooling history and specific entropy of the interior adiabat, can have dramatic effects on the carbon chemistry. Young planets would have quite different abundances (richer in CO) than older planets at the same T_{eq} , all things being equal. We can investigate the role of cooling history on the nitrogen chemistry with these same profiles. In Figure 17 we plot the 1 M_J profiles from 10 Myr to 10

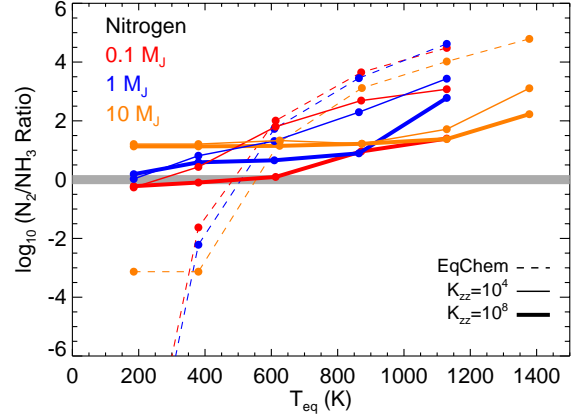


Figure 16. The log of the N_2/NH_3 ratio for 5 values of T_{eq} for 0.1, 1, and 10 M_J model planets, where a subset of the profiles are shown in Figure 15. In equilibrium (at 1 mbar), the transition T_{eq} for $CO/CH_4=1$ ($\log=0$, shaded grey) is at $\sim 420, 530$, and 600 K, from low mass to high mass. This is ~ 400 -500 K colder than the carbon chemistry transitions show in Figure 10. However, vertical mixing essentially flattens the slopes of these curves, as one quenches from high pressure regions that lie on nearly the same adiabat, as shown in Figure 15. For all three model planets, NH_3 exists in detectable amounts for a wide swath of T_{eq} values.

Gyr, this time with the nitrogen quench pressures labeled. The figure is quite similar to 11, but with higher quench pressures, at hotter temperatures. At $\log K_{zz} = 4$, the levels are in the radiative part of the atmosphere, but are relatively pinched together. At $\log K_{zz} = 8$ and 11, we find all quench pressure in or very near the deep atmosphere adiabats.

The effect on the atmospheric mixing ratios of N_2 and NH_3 , shown in Figure 18, are quite straightforward, but different than that found for the carbon chemistry in Figure 12. In equilibrium at 1 mbar, as the atmosphere changes negligibly in temperature, the NH_3 mixing ratio (dashed line) changes little with age. The same is true at $\log K_{zz} = 4$, albeit it at a higher NH_3 abundance. Since both the $\log K_{zz} = 8$ and 11 quench pressures sample the deep adiabat, which are nearly parallel NH_3 abundance curves, we find essentially the *same* behavior of mixing ratio as a function of age, independent of (high) K_{zz} . This is essentially the same as the well-understood brown dwarf behavior.

4.3. Effect of a Mass-Metallicity Relation on Carbon and Nitrogen

So far we have aimed, as much as possible, to investigate the physical and chemical effects of only altering one or two quantities at a time, including distance from the Sun, surface gravity, and T_{int} . Atmospheric

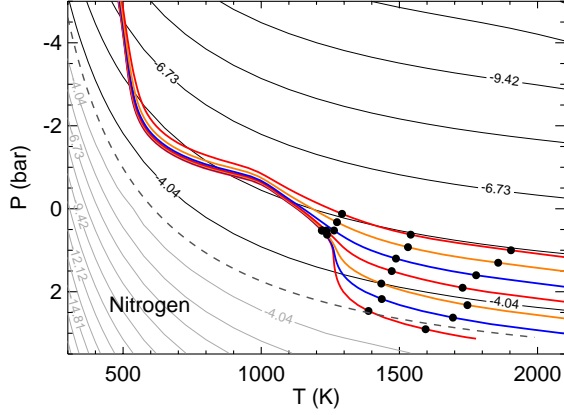


Figure 17. Atmospheric P - T profiles for a $1 M_J$ planet at 0.15 AU from the Sun, assuming $3\times$ solar metallicity. Seven ages, every half dex from 10 Myr to 10 Gyr, with seven values of T_{int} (501, 383, 283, 212, 156, 117, 84 K, from Figure 3) are shown. The three collections of black dots show nitrogen quench pressures for $\log K_{zz} = 4, 8$, and 11 . At depth, all profiles are within the N_2 rich region of P - T space, and the adiabats lie parallel to curves of constant NH_3 abundance.

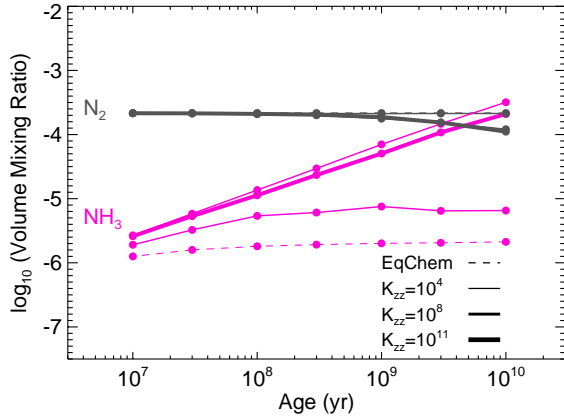


Figure 18. Atmospheric N_2 and NH_3 abundances at 1 mbar as function of planetary age, for the P - T profiles shown in Figure 17. In equilibrium (dashed), the cooling of the planet’s interior has almost no effect on the atmospheric abundances, as the temperatures of the upper atmosphere are essentially constant, and the atmosphere would be N_2 rich. Modest vertical mixing ($\log K_{zz}=4$) yields a slightly higher NH_3 abundance, but still essentially constant with time. More vigorous mixing, from higher quench pressures ($\log K_{zz}$ or 8 and 11), samples progressively more NH_3 -rich gas. However, there is little sensitivity in these models.

metallicity will also play an important role in altering these boundaries. This chemistry has certainly been explored before, or a very wide range of compositions (e.g.,

Moses et al. 2013). In this section we attempt to explore a composition phase space, but in a more narrow sense.

It is strongly suggested from the bulk densities of transiting giant planets that there is a bulk “mass-metallicity relation” for the planets (Thorngren et al. 2016), with the lower mass giant planets being more metal-rich. The effect of such a relation at atmospheric abundances is not yet clear (Kreidberg et al. 2014; Wakeford et al. 2017; Welbanks et al. 2019), but there is such a relation in the solar system for carbon (e.g., Atreya et al. 2016), and from standard models of core-accretion planet formation theory, albeit with a large spread (Fortney et al. 2013).

For both the carbon and nitrogen chemistry discussed in Section 4.1.2 and 4.2.1, for the 3 planet masses at $10\times$ solar, we can examine how an increasing metallicity with lower planet masses may alter the previously examined trends. Figure 19 shows P - T profiles for planets at 0.5 and 2 AU from the Sun, with the upper panel showing carbon quench pressures and the lower panel nitrogen quench pressures. The profiles themselves differ somewhat from those shown in Figure 9 and 15 as the models here use $50\times$ solar ($0.1 M_J$), $3\times$ solar ($1 M_J$), and $1\times$ ($10 M_J$). Since the plots use 3 different metallicities, we also show three different CO/CH_4 equal-abundance curves (dashed).

Compared to our previous investigations into chemistry at $10\times$ solar metallicity (Figures 10 and 16), the two panels in Figure 20 show a much wider range of behavior. At higher metallicity, the cooler models “hang on” to CO and N_2 to much cooler T_{eq} values. In equilibrium the carbon transitions would occur between 1100 and 700 K in these models. Even sluggish vertical mixing shows a large impact. For instance, with more vigorous mixing ($\log K_{zz}=8$), these three transition T_{eq} values are $\sim 1100, 800$, and 450 K.

We can examine the N_2/NH_3 ratio as a function of T_{eq} for these three planets in Figure 19. The crossover T_{eq} for nitrogen chemistry, in equilibrium, would be ~ 600 K at $10 M_J$, 530 K at $1 M_J$, and 420 K at $0.1 M_J$. However, even modest vertical mixing dramatically changes this picture. As the T_{eq} decreases, the quench pressure falls near or into the deep atmosphere adiabat, even at low gravity. On Figure 15 this manifests as the N_2/NH_3 ratio asymptoting to values that depend solely on the metallicity and the specific entropy of the adiabat, as one might have expected for the specific cases investigated for the Saturn-like planet in Figure 14.

4.4. Putting it Together: The Onset of CH_4 and NH_3

We can summarize, at least for the “old” 3-Gyr planets that have been the baseline for many of calculations,

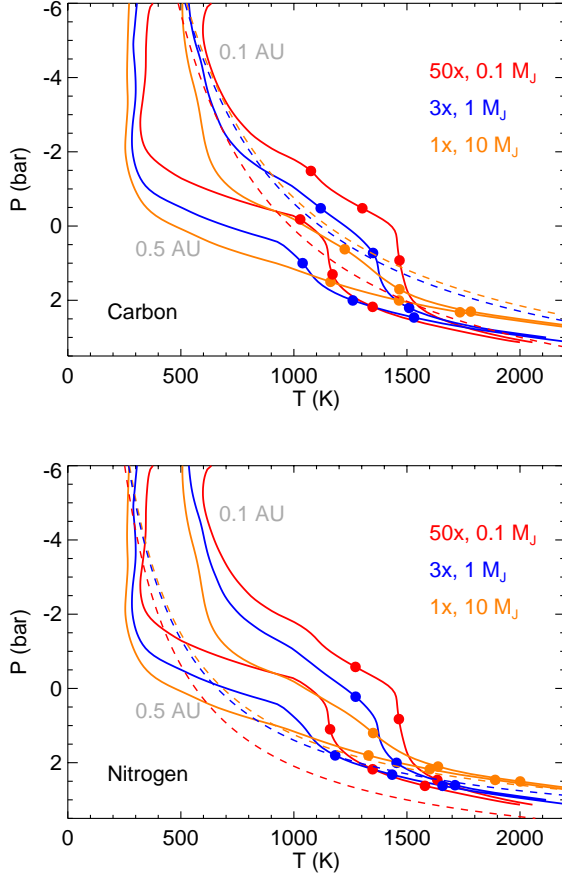


Figure 19. Atmospheric P - T profiles for 3-Gyr-old planets at 0.1 (red, 50 \times), 1 (blue, 3 \times), and 10 (orange, 1 \times) M_J . The CO/CH₄ (upper) and N₂/NH₃ (lower) equal-abundance curves at these 3 metallicity values are shown in dashed curves with the same 3 colors. The models are at 0.1 and 0.5 AU from the Sun. The color-coded dots show the quench pressures for $\log K_{zz} = 4, 8$, and 11 for carbon (upper panel) and nitrogen (lower panel). The nitrogen chemistry quench pressures are at higher pressures than for carbon chemistry. For high gravity and/or cool models, the quench pressure is near or within the deep atmosphere adiabat, in particular for nitrogen.

the expected rise of detectable CH₄ and NH₃ abundances. It is by now well-understood that for the atmospheres of brown dwarfs that the onset of CH₄ and NH₃ are well-separated in T_{eff} -space. Indeed, the rise of near-infrared CH₄ and NH₃ define the T and Y spectral classes, at ~ 1300 K and ~ 600 K respectively (Kirkpatrick 2005; Stephens et al. 2009; Line et al. 2017), although the much stronger mid-IR bands can appear at 1700 K (CH₄ at 3.3 μm) and 1200 K (NH₃ at 10.5 μm).

However, significantly different P - T profiles of irradiated giant planets leads to much different behavior. This

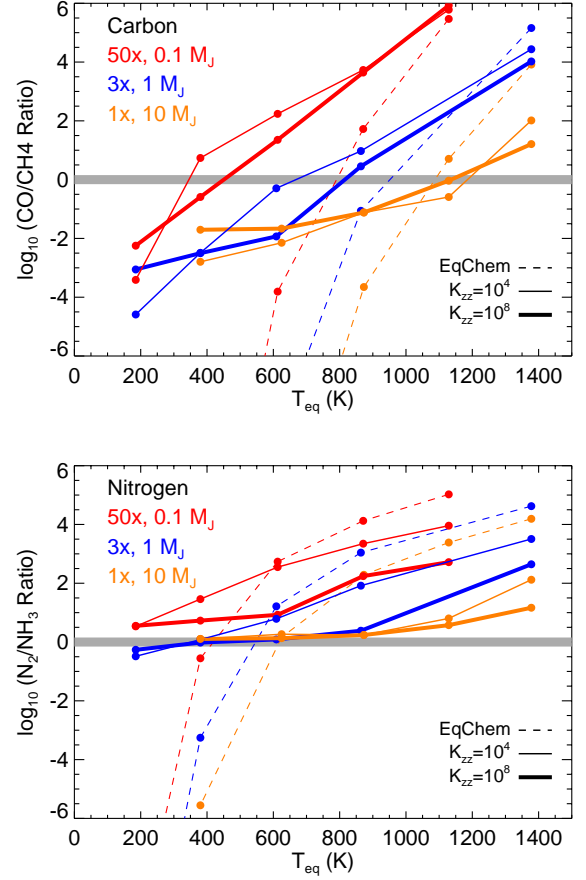


Figure 20. The log of the CO/CH₄ ratio (upper panel) N₂/NH₃ ratio (lower panel) for 5 values of T_{eq} for 0.1, 1, and 10 M_J model planets, where a subset of the profiles are shown in Figure 19. In equilibrium (at 1 mbar), the transition T_{eq} for N₂/NH₃=1 ($\log=0$, shaded grey, lower panel) is at $\sim 420, 530$, and 600 K, from low mass to high mass. This is ~ 400 -500 K colder than the carbon chemistry transitions in the upper panel. For nitrogen in particular, vertical mixing essentially flattens the slopes of these curves, as one quenches from high pressure regions that lie on nearly the same adiabat, as shown in Figure 19. For all three model planets, NH₃ exists in detectable amounts for a wide swath of T_{eq} values.

is shown in Figure 21, both for planets at a fixed 10 \times solar metallicity (top panel) and for planets that use the notional mass-metallicity relation (bottom panel), with both panels using $\log K_{zz}$ of 8. For the higher gravity planets with a large thermal reservoir in their interior, the giant planet behavior is at least similar to that of brown dwarfs, with CH₄ coming on for T_{eq} a few hundred K hotter for the 1 \times solar case at 10 M_J (bottom panel). However, beyond that example, a different and richer behavior, driven mostly by the altered temperature structure of irradiated planets, is seen. For all other

example planets in both panels, CH_4 and NH_3 onset is at a similar T_{eq} , and at the higher metallicities (bottom panel) NH_3 can arise at warmer T_{eq} values than CH_4 .

Figure 21 is in some ways the central prediction of the paper, albeit for a relatively constrained example, as we describe at some length in the Discussion section. The oddly shaped and radiative P - T profiles lead to an expectation of significantly different behavior than that already known for brown dwarfs.

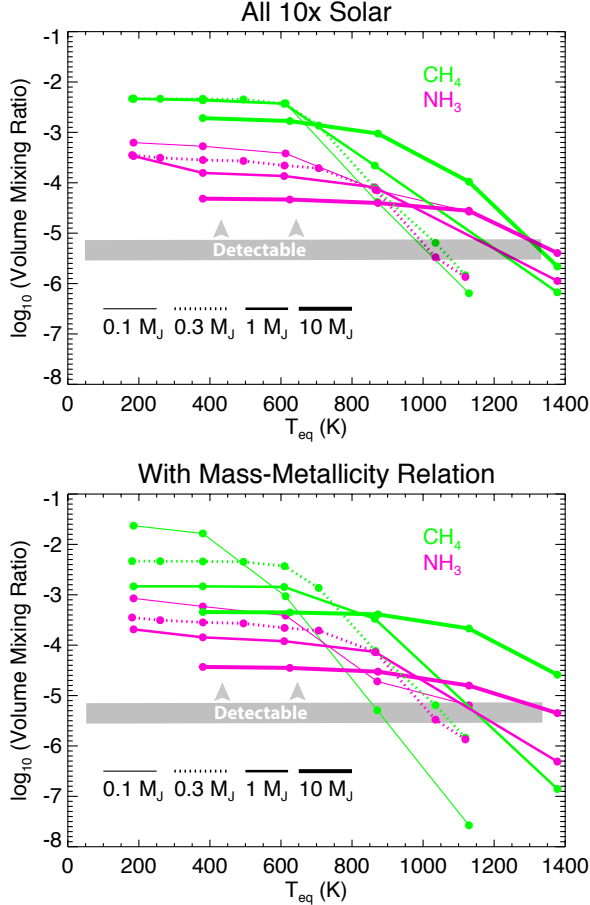


Figure 21. The log of the CH_4 and NH_3 mixing ratios as a function of T_{eq} for models at 0.1, 0.3, 1, and 10 M_J model planets at an age of 3 Gyr. The upper panel shows calculations where $10\times$ solar abundances are used for all models, while the lower panel assumes the mass-metallicity relation (50, 10, 3, and $1\times$ solar) for the 4 masses, respectively. For the range of models, and unlike in brown dwarfs, the onset of NH_3 is nearly coincident with the onset of CH_4 , and for the lower masses ($< 0.3 M_J$), NH_3 onset occurs for warmer T_{eq} values than CH_4 . In this figure $\log K_{zz} = 8$ is assumed.

4.5. Cloud Formation and Cold Traps

A lesson well-learned from observations of transiting planet atmospheres to date is that clouds and hazes can

readily obscure molecular absorption features. This has typically been thought of as a hindrance. However, early work in this field suggested that the atmospheres of giant planets could potentially be classified based on the presence or absence of clouds (Marley et al. 1999; Sudarsky et al. 2000, 2003). In the end, it seems likely that some mixture will be true – in some ways clouds will help us understand temperature structures and transport in these atmospheres, but will also obscure features due to atoms and molecules.

However, it seems clear that the role of clouds will not be a simple function of T_{eq} , as cloud condensation curves can be crossed at a variety of pressures. At a low pressure, perhaps little condensable material will exist. At a high pressure, perhaps all cloud material in an optically thick cloud will be below the visible atmosphere. These effects will depend on the shape of the atmospheric P - T profile, and hence on the specific entropy of the adiabat (which depends on planet mass and age), in addition to the role of atmospheric metallicity (more metals means more cloud-forming material), and even the spectral type of the parent star, which can also alter profile shapes, as discussed below.

In some ways this topic is beyond the scope of the paper, which is focused on 1D models, but we can motivate that there will be a diversity in behavior at a given planetary T_{eq} with plots that focus on P - T profiles and condensation curves. First we will examine our trio of warm Neptunes, GJ 436b, GJ 3470b, and WASP-107b. In Figure 22 we replot the same P - T profiles from Figure 5, with chemical information removed, but now including radiative-convective boundary depths (RCBs) with squares, and condensation curves for potential cloud-forming materials. These “cooler” clouds, for planets cooler than the hot Jupiters, have been studied in Morley et al. (2012, 2013). Note, however, that Gao et al. (2020) have suggested that most of these cloud species (save KCl) may not nucleate and form. Lee et al. (2018) suggest that Cr, KCl, and NaCl (instead of Na_2S) will form across this temperature range. These predictions can be corroborated by future detailed spectroscopic observations of brown dwarfs and planets.

The KCl and ZnS cloud bases move little with or without tidal heating, as the upper atmospheres change little. The Na_2S cloud base, however, can move dramatically. Without tidal heating, the cloud base would be around ~ 300 bars in all three planets. However, for tidal heating with $Q = 10^4$, the Na_2S cloud base moves to ~ 0.1 bar, in the visible atmosphere. A similar effect is seen for MnS and Cr.

We have previously investigated generic Saturn-like-planet P - T profiles at 0.15 AU from the Sun. Figure

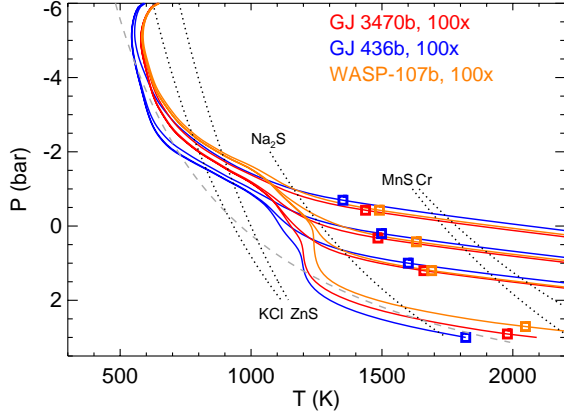


Figure 22. Atmospheric P - T profiles for planets GJ 436b, GJ 3470b, and WASP-107b all at $100\times$ solar abundances, taken from Figure 5. Black dashed curves are for cloud condensation for various elements from Morley et al. (2012). For each planet, 4 interior adiabats are shown, for the case of no tidal heating (coolest), and $Q = 10^6$, 10^5 and 10^4 , from cooler to warmer. Colored squares show the radiative-convective boundary depth. Tidal heating can push cloud formation of Na_2S , MnS , and Cr , out of the deep atmosphere, into the visible atmosphere.

23 shows the same profiles that were explored in Figure 4, now with a focus on RCBs and cloud condensation, rather than chemical abundances. The interface between these profiles and condensation depends strongly on surface gravity. For instance, the denser, higher pressure photosphere of the highest gravity models yields a detached convective zone near 0.2 bar, coincidentally at the region of ZnS and KCl clouds, which is not seen in the lower gravity models. Potentially more vigorous mixing here could lead to thicker clouds and larger particle sizes. If these profiles were calculated at greater orbital distances, yielding cooler atmospheres, all would develop this detached convective zone (Fortney et al. 2007). The Na_2S case is also interesting for these profiles. The cloud base is found in the deep atmosphere for the two higher gravity models, but at a few tenths of bar in the three lower gravity models. This clearly shows that at a given T_{eq} , the depth of cloud formation can be significantly impacted by temperature of the deep atmosphere, which is mitigated by the interior cooling. One could readily imagine other examples where the cloud formation depth is affected by planetary age, at a given mass, as is seen in brown dwarfs and self-luminous imaged planets.

5. DISCUSSION

We wish to stress that the calculations shown here are only a starting point, and we have considered only what

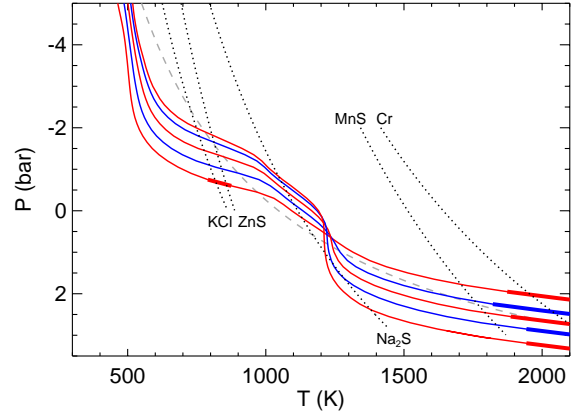


Figure 23. Model pressure-temperature profile for a $10\times$ solar atmosphere at 0.15 AU from the Sun. The five profiles from Figure 4 show (alternating red and blue) five values of T_{int} , at 52, 77, 117, 182, and 333 K, with respective surface gravities $g=5.8, 9.8, 24, 65$, and 225 m s^{-2} . Thicker parts of the profiles show convective regions. Note that the specific entropy of the deep atmosphere adiabat can move the location of the Na_2S cloud into the visible atmosphere (base 1 bar for the highest gravity model) or a depth (base at 300 bar in the lowest gravity model). The high gravity model also has a detached convective zone (coincidentally) at the location of ZnS and KCl condensate formation.

we believe will be the 1st order effects. In the interest of brevity we have not considered several additional factors that could or will play important roles in further altering predicted temperature structures and atmospheric abundances. We describe these here:

1. We have elected not to self-consistently recalculate the atmospheric P - T profiles for each value of K_{zz} . The altered atmospheric abundances in turn alter the radiative-convective equilibrium profile, as has been explored by several authors, with and without stellar irradiation (Hubeny & Burrows 2007; Drummond et al. 2018a; Phillips et al. 2020). In particular Drummond et al. (2018a), for HD 189733b and HD 209458b, found differences in the P - T profile of up to 100 K. For the arguments presented here, tripling or quadrupling the number of plotted P - T profiles (one for every K_{zz}) would distract from the main point, particularly given the large uncertainty today in the K_{zz} profiles. Additionally, including the cloud species discussed here would alter P - T profiles and chemical transitions (Molaverdikhani et al. 2020).
2. We have assumed a constant value of K_{zz} with height. Mixing length theory is an important guide to K_{zz} in convective regions, but it is not

- yet clear how K_{zz} transitions at the radiative-convective boundary, in particular given the 3D nature of atmospheric mixing. Three-dimensional GCM runs may be a guide for particular planets of interest. Work to date has suggested that as one moves deeper, to higher pressures in the radiative regions, that K_{zz} should decrease. This may lead to a “quench bottle neck” of less vigorous mixing just above the RCB.
3. Our models are 1D, however 3D effects have been shown to be important in understanding atmospheric abundances. As has previously been demonstrated (Cooper & Showman 2006; Agúndez et al. 2014; Drummond et al. 2018b, 2020), non-equilibrium chemistry is affected by day-night temperature differences in addition to vertical mixing. Day-night effects *may* be minimized for these relatively cooler planets, compared to the hot Jupiters, as day-night temperature differences are expected to be more modest at cooler temperatures (Lewis et al. 2010; Perez-Becker & Showman 2013).
 4. Non-solar ratios of elemental abundance ratios are likely to occur. As has been extensively modeled over the past decade, planet formation processes can drive atmospheres towards higher or lower C/O ratios, depending on the formation location and the relative accretion of solids and gas (e.g., Öberg et al. 2011; Madhusudhan et al. 2014; Mordasini et al. 2016; Espinoza et al. 2017). More recently, the role of the nitrogen N_2 ice line as a site of planet formation (Piso et al. 2016; Bosman et al. 2019; Öberg & Wordsworth 2019) and altered N/O and N/C ratios in giant planet atmospheres (Cridland et al. 2020) has been investigated. Previous radiative-convective atmospheric calculations have shown that an altered C/O ratio can alter P - T phase space of major chemical transitions (e.g., Madhusudhan et al. 2011b; Mollière et al. 2015).
 5. Photochemistry will further alter atmospheric abundances. The nonequilibrium abundances that we find, based on timescale arguments, are merely the “raw materials” for further chemical reactions (Zahnle et al. 2009b,a; Moses et al. 2011, 2013; Venot et al. 2020). It is well known that CH_4 in the solar system can be readily photolyzed, and the destruction of CH_4 may make it less easily observed, while increasing the abundances of other hydrocarbons, along with photochemical hazes. We note that signs of hazes may already be seen in the transmission spectra of the cool transiting giant planet population (Gao et al. 2020).
 6. A range of parent star spectral types will be relevant across the planetary population. Moving from hot stars to cool stars, the peak of the stellar spectral energy distribution moves to redder wavelengths, and the temperature of the incoming radiation field is more similar to that of the planetary atmosphere, leading to more isothermal temperature structure (Mollière et al. 2015), as shown in Figure 24. The range from hotter to cooler parent stars certainly spans at least the range from F to M. Temperature differences of ~ 150 K are seen at at 1-100 bars, the relevant quench pressures for $\log K_{zz}=8$, which straddles the CO/ CH_4 equal abundance curve. Interestingly, this could be a very nice probe of K_{zz} , as for this example, as much lower and much higher K_{zz} values, the profiles converge back to similar CO/ CH_4 abundances.
 7. A range of planetary eccentricities can impact the timescale arguments made here, as well as drive tidal heating. The thermal response of the planetary atmospheric temperatures, and hence chemistry, depends on the planetary orbit. The timescale over which the atmosphere heats up and cools off due to the eccentric orbit will compete with the timescales t_{mix} and t_{chem} that we have explored here. This idea was previously explored for highly eccentric hot Jupiters by Visscher (2012), but a new study that focuses on cooler planets appears to be warranted. Tidal heating from the interior, as shown for planets GJ 436b, GJ 3470b, and WASP-107b in Section 3, should be a relatively common process, particularly for the “in-between” planets that are not so close that they will have circularized quickly, and are not so far tides do not affect the energy budget. Tidal heating should then be investigated for any particular target of interest. Assessing the eccentricity of a given planet may be difficult, if radial velocity data is sparse, or if a secondary eclipse is not detected.
 8. The radius-inflation mechanism that affects hot Jupiters may still operate in the cooler planets we investigate here. Since Thorngren & Fortney (2018) and Thorngren et al. (2019), found no strong evidence for the mechanism affecting planets cooler than $T_{\text{eq}} < 1000$ K, we have used standard thermal evolution models that lack additional heating. However, modest additional internal heating could warm the deep atmosphere, with

only small effects on the observed radius vs. incident flux distribution, which would be currently undetectable in the planetary population. And any “residual” radius inflation power could be important for the Saturn- and Neptune-class planets, whose interiors would be expected to cool of significantly in the absence of additional power. This would lead to lower CH_4/CO and NH_3/N_2 ratios at a given T_{eq} , compared to our calculations, and could be an important probe of temperatures in the deeper atmosphere.

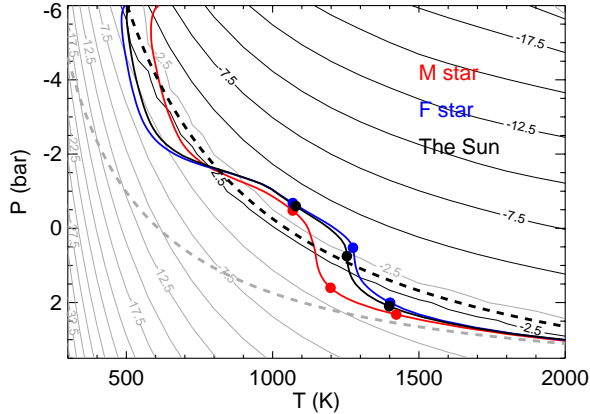


Figure 24. Atmospheric P - T profiles for three planets with the same incident stellar flux. For the profile in black, the planet is at 0.15 AU. In red is a profile with the GJ 436b parent star (type M2.5), while in blue it is the WASP-17b parent star (type F4). Here $\log K_{zz}$ values of 4, 8, and 11 are shown as upper, middle, and lower set of color dots, respectively. Large temperature differences are particularly seen at 1–100 bars, the relevant quench pressures for $\log K_{zz}=8$, which straddles the CO/CH_4 equal abundance curve (dashed black). The N_2/NH_3 equal abundance curve is shown in dashed gray, for reference.

6. CONCLUSIONS

Through a straightforward implementation of 1D radiative-convective model atmospheres and non-equilibrium chemistry, we have shown that atmospheric abundances of C-, N-, and O-bearing molecules in warm transiting planets will show a diverse and complex behavior. This behavior will depend strongly on the cooling history of the planet, such that a planet’s mass, age, parent star spectral type, and any ongoing tidal dissipation can lead to atmospheric abundances that differ from planet to planet at the same level of incident stellar flux.

Non-equilibrium chemical abundances may then serve as a tool to probe the deeper atmosphere, similar to work

recently begun for very cool brown dwarfs (Miles et al. 2020). For the three Neptune-class planets discussed in Section 3 (GJ 436b, GJ 3480b, and WASP-107b), we suggest that ongoing eccentricity damping tidally heats the deep atmospheres of the planets. This raises temperatures by several thousand degrees and drives strong convective mixing, which dramatically decreases the CH_4/CO ratio in the visible atmosphere. This may play the dominant role in understanding their observations to date.

The more isothermal shape of P - T profiles in irradiated planets, compared to brown dwarfs, leads to the expectation that planetary behavior will differ strongly compared to brown dwarfs. Perhaps most strikingly, the onset of detectable CH_4 and then NH_3 should occur at very similar T_{eq} values, and for the Saturn-masses and below, a reversal compared to brown dwarf behavior, where NH_3 is seen at warmer temperatures than CH_4 . We have also shown that N_2 will dominate over NH_3 over a wide range of temperatures and ages, such that bulk nitrogen abundances determined from NH_3 will only be lower limits.

To discover the underlying physical and chemical trends for these atmospheres, it would likely be the most straightforward to look for *trends at a given mass and age*. For instance, in mature planetary systems (say, Gyr+), the Jupiter-mass planets around Sunlike stars at $T_{\text{eq}} < 1000$ K would all be expected (barring tidal heating) to have T_{int} values of ~ 100 K. One could expect to see a trend of increasing CH_4 abundance with lower T_{eq} , with CH_4 becoming dominant at 800 K, as in Figure 10. Note, however, that this potential trend could readily be disguised by mixing planets with a range of masses into one’s sample, as shown in that same figure. We reiterate that it is not yet known how diverse the atmospheric metallicities of those planets may be, and how that may change with planetary mass, which would also add scatter to any trend.

While retrievals to constrain atmospheric abundances and temperature structures (see Madhusudhan 2018, for a review) are likely up to the task for determining abundances in planetary transmission and emission, these findings can only properly be interpreted *within the context of the physical characteristics of the planet and its environment*. In particular, since we find that T_{int} can play a significant role in altering abundances, retrievals that utilize deep atmospheric temperatures that are guided by thermal (and/or tidal) evolution models, and aim to retrieve the quench pressure depth in addition to molecular mixing ratios, may yield the most robust results. The role of planetary structure modeling, thermal evolution modeling, and physics-driven 1D

and 3D models, to complement retrieval, are essential to interpreting observations.

ACKNOWLEDGMENTS

JJF wishes to dedicate this paper to Adam P. Showman, a great scientist, long-time collaborator, and good friend. The authors thank Caroline Morley and Jacob Bean for insightful discussions during the course of this project. JJF, MSM, MRL, RSF, and RL acknowledge the support of NASA Exoplanets Research Program grant 80NSSC19K0446.

REFERENCES

- Agúndez, M., Parmentier, V., Venot, O., Hersant, F., & Selsis, F. 2014, *A&A*, 564, A73, doi: [10.1051/0004-6361/201322895](https://doi.org/10.1051/0004-6361/201322895)
- Artigau, É. 2018, *Variability of Brown Dwarfs*, 94, doi: [10.1007/978-3-319-55333-7_94](https://doi.org/10.1007/978-3-319-55333-7_94)
- Atreya, S. K., Crida, A., Guillot, T., et al. 2016, arXiv e-prints, arXiv:1606.04510. <https://arxiv.org/abs/1606.04510>
- Baraffe, I., Chabrier, G., & Barman, T. 2008, *A&A*, 482, 315, doi: [10.1051/0004-6361:20079321](https://doi.org/10.1051/0004-6361:20079321)
- Beatty, T. G., Marley, M. S., Gaudi, B. S., et al. 2019, *AJ*, 158, 166, doi: [10.3847/1538-3881/ab33fc](https://doi.org/10.3847/1538-3881/ab33fc)
- Beatty, T. G., Collins, K. A., Fortney, J., et al. 2014, *ApJ*, 783, 112, doi: [10.1088/0004-637X/783/2/112](https://doi.org/10.1088/0004-637X/783/2/112)
- Beichman, C., Benneke, B., Knutson, H., et al. 2014, *PASP*, 126, 1134, doi: [10.1086/679566](https://doi.org/10.1086/679566)
- Benneke, B., Knutson, H. A., Lothringer, J., et al. 2019, *Nature Astronomy*, 3, 813, doi: [10.1038/s41550-019-0800-5](https://doi.org/10.1038/s41550-019-0800-5)
- Berardo, D., & Cumming, A. 2017, *ApJL*, 846, L17, doi: [10.3847/2041-8213/aa81c0](https://doi.org/10.3847/2041-8213/aa81c0)
- Bosman, A. D., Cridland, A. J., & Miguel, Y. 2019, *A&A*, 632, L11, doi: [10.1051/0004-6361/201936827](https://doi.org/10.1051/0004-6361/201936827)
- Bowler, B. P. 2016, *PASP*, 128, 102001, doi: [10.1088/1538-3873/128/968/102001](https://doi.org/10.1088/1538-3873/128/968/102001)
- Burrows, A., Hubbard, W. B., Lunine, J. I., & Liebert, J. 2001, *Reviews of Modern Physics*, 73, 719. http://adsabs.harvard.edu/cgi-bin/nph-bib_query?bibcode=2001RvMP...73..719B&db_key=AST
- Burrows, A., Hubeny, I., Budaj, J., Knutson, H. A., & Charbonneau, D. 2007, *ApJL*, 668, L171, doi: [10.1086/522834](https://doi.org/10.1086/522834)
- Burrows, A., Marley, M., Hubbard, W. B., et al. 1997, *ApJ*, 491, 856
- Chabrier, G., & Baraffe, I. 2000, *ARA&A*, 38, 337
- Cooper, C. S., & Showman, A. P. 2006, *ApJ*, 649, 1048, doi: [10.1086/506312](https://doi.org/10.1086/506312)
- Cridland, A. J., van Dishoeck, E. F., Alessi, M., & Pudritz, R. E. 2020, arXiv e-prints, arXiv:2009.02907. <https://arxiv.org/abs/2009.02907>
- Cushing, M. C., Roellig, T. L., Marley, M. S., et al. 2006, *ApJ*, 648, 614, doi: [10.1086/505637](https://doi.org/10.1086/505637)
- Dransfield, G., & Triaud, A. H. M. J. 2020, arXiv e-prints, arXiv:2008.00995. <https://arxiv.org/abs/2008.00995>
- Drummond, B., Mayne, N. J., Baraffe, I., et al. 2018a, *A&A*, 612, A105, doi: [10.1051/0004-6361/201732010](https://doi.org/10.1051/0004-6361/201732010)
- Drummond, B., Mayne, N. J., Manners, J., et al. 2018b, *ApJ*, 869, 28, doi: [10.3847/1538-4357/aaeb28](https://doi.org/10.3847/1538-4357/aaeb28)
- Drummond, B., Hébrard, E., Mayne, N. J., et al. 2020, *A&A*, 636, A68, doi: [10.1051/0004-6361/201937153](https://doi.org/10.1051/0004-6361/201937153)
- Espinoza, N., Fortney, J. J., Miguel, Y., Thorngren, D., & Murray-Clay, R. 2017, *ApJL*, 838, L9, doi: [10.3847/2041-8213/aa65ca](https://doi.org/10.3847/2041-8213/aa65ca)
- Fegley, B. J., & Lodders, K. 1996, *ApJL*, 472, L37
- Fortney, J. J., Lodders, K., Marley, M. S., & Freedman, R. S. 2008, *ApJ*, 678, 1419, doi: [10.1086/528370](https://doi.org/10.1086/528370)
- Fortney, J. J., Marley, M. S., & Barnes, J. W. 2007, *ApJ*, 659, 1661, doi: [10.1086/512120](https://doi.org/10.1086/512120)
- Fortney, J. J., Marley, M. S., Lodders, K., Saumon, D., & Freedman, R. 2005, *ApJL*, 627, L69, doi: [10.1086/431952](https://doi.org/10.1086/431952)
- Fortney, J. J., Mordasini, C., Nettelmann, N., et al. 2013, *ApJ*, 775, 80, doi: [10.1088/0004-637X/775/1/80](https://doi.org/10.1088/0004-637X/775/1/80)
- Fortney, J. J., Thorngren, D., Line, M. R., & Morley, C. 2017, in *AAS/Division for Planetary Sciences Meeting Abstracts #49*, AAS/Division for Planetary Sciences Meeting Abstracts, 408.04
- Freedman, R. S., Lustig-Yaeger, J., Fortney, J. J., et al. 2014, *ApJS*, 214, 25, doi: [10.1088/0067-0049/214/2/25](https://doi.org/10.1088/0067-0049/214/2/25)
- Gao, P., Thorngren, D. P., Lee, G. K. H., et al. 2020, *Nature Astronomy*, doi: [10.1038/s41550-020-1114-3](https://doi.org/10.1038/s41550-020-1114-3)
- Garhart, E., Deming, D., Mandell, A., et al. 2020, *AJ*, 159, 137, doi: [10.3847/1538-3881/ab6c6f](https://doi.org/10.3847/1538-3881/ab6c6f)
- Gierasch, P. J., & Conrath, B. J. 1985, *Energy conversion processes in the outer planets.*, ed. G. E. Hunt, 121–146

- Gillon, M., Pont, F., Demory, B.-O., et al. 2007, *A&A*, 472, L13, doi: [10.1051/0004-6361:20077799](https://doi.org/10.1051/0004-6361:20077799)
- Gravity Collaboration, Lacour, S., Nowak, M., et al. 2019, *A&A*, 623, L11, doi: [10.1051/0004-6361/201935253](https://doi.org/10.1051/0004-6361/201935253)
- Greene, T. P., Line, M. R., Montero, C., et al. 2016, *ApJ*, 817, 17, doi: [10.3847/0004-637X/817/1/17](https://doi.org/10.3847/0004-637X/817/1/17)
- Guillot, T. 2010, *A&A*, 520, A27, doi: [10.1051/0004-6361/200913396](https://doi.org/10.1051/0004-6361/200913396)
- Helling, C., & Casewell, S. 2014, *A&A Rv*, 22, 80, doi: [10.1007/s00159-014-0080-0](https://doi.org/10.1007/s00159-014-0080-0)
- Hubeny, I., & Burrows, A. 2007, *ApJ*, 669, 1248
- Kammer, J. A., Knutson, H. A., Line, M. R., et al. 2015, *ApJ*, 810, 118, doi: [10.1088/0004-637X/810/2/118](https://doi.org/10.1088/0004-637X/810/2/118)
- Kirkpatrick, J. D. 2005, *ARA&A*, 43, 195
- Konopacky, Q. M., Barman, T. S., Macintosh, B. A., & Marois, C. 2013, *Science*, 339, 1398, doi: [10.1126/science.1232003](https://doi.org/10.1126/science.1232003)
- Kreidberg, L., Line, M. R., Thorngren, D., Morley, C. V., & Stevenson, K. B. 2018, *ApJL*, 858, L6, doi: [10.3847/2041-8213/aabfce](https://doi.org/10.3847/2041-8213/aabfce)
- Kreidberg, L., Bean, J. L., Désert, J.-M., et al. 2014, *ApJL*, 793, L27, doi: [10.1088/2041-8205/793/2/L27](https://doi.org/10.1088/2041-8205/793/2/L27)
- Leconte, J., Chabrier, G., Baraffe, I., & Levrard, B. 2010, *A&A*, 516, A64, doi: [10.1051/0004-6361/201014337](https://doi.org/10.1051/0004-6361/201014337)
- Lee, G. K. H., Blecic, J., & Helling, C. 2018, *A&A*, 614, A126, doi: [10.1051/0004-6361/201731977](https://doi.org/10.1051/0004-6361/201731977)
- Lewis, N. K., Showman, A. P., Fortney, J. J., et al. 2010, *ApJ*, 720, 344, doi: [10.1088/0004-637X/720/1/344](https://doi.org/10.1088/0004-637X/720/1/344)
- Li, L., Jiang, X., West, R. A., et al. 2018, *Nature Communications*, 9, 3709, doi: [10.1038/s41467-018-06107-2](https://doi.org/10.1038/s41467-018-06107-2)
- Line, M. R., Marley, M. S., Liu, M. C., et al. 2017, *ApJ*, 848, 83, doi: [10.3847/1538-4357/aa7ff0](https://doi.org/10.3847/1538-4357/aa7ff0)
- Lodders, K., & Fegley, B. 2002, *Icarus*, 155, 393
- Luhman, K. L. 2014, *ApJL*, 786, L18, doi: [10.1088/2041-8205/786/2/L18](https://doi.org/10.1088/2041-8205/786/2/L18)
- Lupu, R. E., Zahnle, K., Marley, M. S., et al. 2014, *ApJ*, 784, 27, doi: [10.1088/0004-637X/784/1/27](https://doi.org/10.1088/0004-637X/784/1/27)
- Macintosh, B., Graham, J. R., Barman, T., et al. 2015, *Science*, 350, 64, doi: [10.1126/science.aac5891](https://doi.org/10.1126/science.aac5891)
- Madhusudhan, N. 2018, *Atmospheric Retrieval of Exoplanets*, 104, doi: [10.1007/978-3-319-55333-7_104](https://doi.org/10.1007/978-3-319-55333-7_104)
- Madhusudhan, N., Amin, M. A., & Kennedy, G. M. 2014, *ApJL*, 794, L12, doi: [10.1088/2041-8205/794/1/L12](https://doi.org/10.1088/2041-8205/794/1/L12)
- Madhusudhan, N., Mousis, O., Johnson, T. V., & Lunine, J. I. 2011a, *ApJ*, 743, 191, doi: [10.1088/0004-637X/743/2/191](https://doi.org/10.1088/0004-637X/743/2/191)
- Madhusudhan, N., Harrington, J., Stevenson, K. B., et al. 2011b, *Nature*, 469, 64, doi: [10.1038/nature09602](https://doi.org/10.1038/nature09602)
- Marley, M. S., Fortney, J., Seager, S., & Barman, T. 2007, in *Protostars and Planets V*, ed. B. Reipurth, D. Jewitt, & K. Keil, 733–747
- Marley, M. S., Gelino, C., Stephens, D., Lunine, J. I., & Freedman, R. 1999, *ApJ*, 513, 879
- Marley, M. S., & McKay, C. P. 1999, *Icarus*, 138, 268
- Marley, M. S., & Robinson, T. D. 2015, *ARA&A*, 53, 279, doi: [10.1146/annurev-astro-082214-122522](https://doi.org/10.1146/annurev-astro-082214-122522)
- Marley, M. S., Saumon, D., Guillot, T., et al. 1996, *Science*, 272, 1919
- Mayor, M., & Queloz, D. 1995, *Nature*, 378, 355
- McKay, C. P., Pollack, J. B., & Courtin, R. 1989, *Icarus*, 80, 23
- Menou, K. 2019, *MNRAS*, 485, L98, doi: [10.1093/mnrasl/slz041](https://doi.org/10.1093/mnrasl/slz041)
- Miguel, Y., & Kaltenegger, L. 2014, *ApJ*, 780, 166, doi: [10.1088/0004-637X/780/2/166](https://doi.org/10.1088/0004-637X/780/2/166)
- Miles, B. E., Skemer, A. J. I., Morley, C. V., et al. 2020, *AJ*, 160, 63, doi: [10.3847/1538-3881/ab9114](https://doi.org/10.3847/1538-3881/ab9114)
- Molaverdikhani, K., Henning, T., & Mollière, P. 2019, *ApJ*, 883, 194, doi: [10.3847/1538-4357/ab3e30](https://doi.org/10.3847/1538-4357/ab3e30)
- . 2020, *ApJ*, 899, 53, doi: [10.3847/1538-4357/aba52b](https://doi.org/10.3847/1538-4357/aba52b)
- Mollière, P., van Boekel, R., Dullemond, C., Henning, T., & Mordasini, C. 2015, *ApJ*, 813, 47, doi: [10.1088/0004-637X/813/1/47](https://doi.org/10.1088/0004-637X/813/1/47)
- Mordasini, C., van Boekel, R., Mollière, P., Henning, T., & Benneke, B. 2016, *ApJ*, 832, 41, doi: [10.3847/0004-637X/832/1/41](https://doi.org/10.3847/0004-637X/832/1/41)
- Morley, C. V., Fortney, J. J., Marley, M. S., et al. 2012, *ApJ*, 756, 172, doi: [10.1088/0004-637X/756/2/172](https://doi.org/10.1088/0004-637X/756/2/172)
- . 2013, *ApJ*, 756, 172, doi: [10.1088/0004-637X/756/2/172](https://doi.org/10.1088/0004-637X/756/2/172)
- Morley, C. V., Knutson, H., Line, M., et al. 2017a, *AJ*, 153, 86, doi: [10.3847/1538-3881/153/2/86](https://doi.org/10.3847/1538-3881/153/2/86)
- Morley, C. V., Kreidberg, L., Rustamkulov, Z., Robinson, T., & Fortney, J. J. 2017b, *ApJ*, 850, 121, doi: [10.3847/1538-4357/aa927b](https://doi.org/10.3847/1538-4357/aa927b)
- Moses, J. I., Visscher, C., Fortney, J. J., et al. 2011, *ApJ*, 737, 15, doi: [10.1088/0004-637X/737/1/15](https://doi.org/10.1088/0004-637X/737/1/15)
- Moses, J. I., Line, M. R., Visscher, C., et al. 2013, *ApJ*, 777, 34, doi: [10.1088/0004-637X/777/1/34](https://doi.org/10.1088/0004-637X/777/1/34)
- Öberg, K. I., Murray-Clay, R., & Bergin, E. A. 2011, *ApJL*, 743, L16, doi: [10.1088/2041-8205/743/1/L16](https://doi.org/10.1088/2041-8205/743/1/L16)
- Öberg, K. I., & Wordsworth, R. 2019, *AJ*, 158, 194, doi: [10.3847/1538-3881/ab46a8](https://doi.org/10.3847/1538-3881/ab46a8)
- Parmentier, V., & Crossfield, I. J. M. 2018, *Exoplanet Phase Curves: Observations and Theory*, 116, doi: [10.1007/978-3-319-55333-7_116](https://doi.org/10.1007/978-3-319-55333-7_116)
- Parmentier, V., Showman, A. P., & Lian, Y. 2013, *A&A*, 558, A91, doi: [10.1051/0004-6361/201321132](https://doi.org/10.1051/0004-6361/201321132)

- Pearl, J. C., & Conrath, B. J. 1991, *J. Geophys. Res.*, 96, 18921
- Perez-Becker, D., & Showman, A. P. 2013, *ApJ*, 776, 134, doi: [10.1088/0004-637X/776/2/134](https://doi.org/10.1088/0004-637X/776/2/134)
- Phillips, M. W., Tremblin, P., Baraffe, I., et al. 2020, *A&A*, 637, A38, doi: [10.1051/0004-6361/201937381](https://doi.org/10.1051/0004-6361/201937381)
- Piso, A.-M. A., Pegues, J., & Öberg, K. I. 2016, *ApJ*, 833, 203, doi: [10.3847/1538-4357/833/2/203](https://doi.org/10.3847/1538-4357/833/2/203)
- Prinn, R. G., & Barshay, S. S. 1977, *Science*, 198, 1031
- Saumon, D., Chabrier, G., & van Horn, H. M. 1995, *ApJS*, 99, 713
- Saumon, D., Geballe, T. R., Leggett, S. K., et al. 2000, *ApJ*, 541, 374
- Saumon, D., Marley, M. S., Cushing, M. C., et al. 2006, *ApJ*, 647, 552, doi: [10.1086/505419](https://doi.org/10.1086/505419)
- Saumon, D., Marley, M. S., Lodders, K., & Freedman, R. S. 2003, in *Brown Dwarfs, Proceedings of IAU Symposium #211*, ed. E. Martin, (San Francisco: Astronomical Society of the Pacific), 345
- Sing, D. K., Fortney, J. J., Nikolov, N., et al. 2016, *Nature*, 529, 59, doi: [10.1038/nature16068](https://doi.org/10.1038/nature16068)
- Sing, D. K., Lavvas, P., Ballester, G. E., et al. 2019, *AJ*, 158, 91, doi: [10.3847/1538-3881/ab2986](https://doi.org/10.3847/1538-3881/ab2986)
- Skemer, A. J., Morley, C. V., Allers, K. N., et al. 2016, *ApJL*, 826, L17, doi: [10.3847/2041-8205/826/2/L17](https://doi.org/10.3847/2041-8205/826/2/L17)
- Smith, M. D. 1998, *Icarus*, 132, 176, doi: [10.1006/icar.1997.5886](https://doi.org/10.1006/icar.1997.5886)
- Stephens, D. C., Leggett, S. K., Cushing, M. C., et al. 2009, *ApJ*, 702, 154, doi: [10.1088/0004-637X/702/1/154](https://doi.org/10.1088/0004-637X/702/1/154)
- Stevenson, K. B., Harrington, J., Nymeyer, S., et al. 2010, *Nature*, 464, 1161, doi: [10.1038/nature09013](https://doi.org/10.1038/nature09013)
- Sudarsky, D., Burrows, A., & Hubeny, I. 2003, *ApJ*, 588, 1121
- Sudarsky, D., Burrows, A., & Pinto, P. 2000, *ApJ*, 538, 885. http://adsabs.harvard.edu/cgi-bin/nph-bib_query?bibcode=2000ApJ...538..885S&db.key=AST
- Thorngren, D., Gao, P., & Fortney, J. J. 2019, *ApJL*, 884, L6, doi: [10.3847/2041-8213/ab43d0](https://doi.org/10.3847/2041-8213/ab43d0)
- . 2020, *ApJL*, 889, L39, doi: [10.3847/2041-8213/ab6d6c](https://doi.org/10.3847/2041-8213/ab6d6c)
- Thorngren, D. P., & Fortney, J. J. 2018, *AJ*, 155, 214, doi: [10.3847/1538-3881/aaba13](https://doi.org/10.3847/1538-3881/aaba13)
- Thorngren, D. P., Fortney, J. J., Murray-Clay, R. A., & Lopez, E. D. 2016, *ApJ*, 831, 64, doi: [10.3847/0004-637X/831/1/64](https://doi.org/10.3847/0004-637X/831/1/64)
- Tinetti, G., Drossart, P., Eccleston, P., et al. 2018, *Experimental Astronomy*, 46, 135, doi: [10.1007/s10686-018-9598-x](https://doi.org/10.1007/s10686-018-9598-x)
- Triaud, A. H. M. J., Gillon, M., Ehrenreich, D., et al. 2015, *MNRAS*, 450, 2279, doi: [10.1093/mnras/stv706](https://doi.org/10.1093/mnras/stv706)
- Vazan, A., Helled, R., Kovetz, A., & Podolak, M. 2015, *ApJ*, 803, 32, doi: [10.1088/0004-637X/803/1/32](https://doi.org/10.1088/0004-637X/803/1/32)
- Venot, O., Cavalié, T., Bounaceur, R., et al. 2020, *A&A*, 634, A78, doi: [10.1051/0004-6361/201936697](https://doi.org/10.1051/0004-6361/201936697)
- Venot, O., Hébrard, E., Agúndez, M., et al. 2012, *A&A*, 546, A43, doi: [10.1051/0004-6361/201219310](https://doi.org/10.1051/0004-6361/201219310)
- Visscher, C. 2012, *ApJ*, 757, 5, doi: [10.1088/0004-637X/757/1/5](https://doi.org/10.1088/0004-637X/757/1/5)
- Visscher, C., Lodders, K., & Fegley, Jr., B. 2010, *ApJ*, 716, 1060, doi: [10.1088/0004-637X/716/2/1060](https://doi.org/10.1088/0004-637X/716/2/1060)
- Visscher, C., Lodders, K., & Fegley, B. J. 2006, *ApJ*, 648, 1181, doi: [10.1086/506245](https://doi.org/10.1086/506245)
- Visscher, C., & Moses, J. I. 2011, *ApJ*, 738, 72, doi: [10.1088/0004-637X/738/1/72](https://doi.org/10.1088/0004-637X/738/1/72)
- Vos, J. M., Allers, K. N., & Biller, B. A. 2017, *ApJ*, 842, 78, doi: [10.3847/1538-4357/aa73cf](https://doi.org/10.3847/1538-4357/aa73cf)
- Wakeford, H. R., Sing, D. K., Kataria, T., et al. 2017, *Science*, 356, 628, doi: [10.1126/science.aah4668](https://doi.org/10.1126/science.aah4668)
- Wallack, N. L., Knutson, H. A., Morley, C. V., et al. 2019, *AJ*, 158, 217, doi: [10.3847/1538-3881/ab2a05](https://doi.org/10.3847/1538-3881/ab2a05)
- Welbanks, L., Madhusudhan, N., Allard, N. F., et al. 2019, *ApJL*, 887, L20, doi: [10.3847/2041-8213/ab5a89](https://doi.org/10.3847/2041-8213/ab5a89)
- Wong, M. H., Mahaffy, P. R., Atreya, S. K., Niemann, H. B., & Owen, T. C. 2004, *Icarus*, 171, 153, doi: [10.1016/j.icarus.2004.04.010](https://doi.org/10.1016/j.icarus.2004.04.010)
- Zahnle, K., Marley, M. S., & Fortney, J. J. 2009a, *ArXiv e-prints*. <https://arxiv.org/abs/0911.0728>
- Zahnle, K., Marley, M. S., Freedman, R. S., Lodders, K., & Fortney, J. J. 2009b, *ApJL*, 701, L20, doi: [10.1088/0004-637X/701/1/L20](https://doi.org/10.1088/0004-637X/701/1/L20)
- Zahnle, K. J., & Marley, M. S. 2014, *ApJ*, 797, 41, doi: [10.1088/0004-637X/797/1/41](https://doi.org/10.1088/0004-637X/797/1/41)
- Zhang, K., & Hamilton, D. P. 2008, *Icarus*, 193, 267, doi: [10.1016/j.icarus.2007.08.024](https://doi.org/10.1016/j.icarus.2007.08.024)
- Zhang, X., & Showman, A. P. 2018a, *ApJ*, 866, 1, doi: [10.3847/1538-4357/aada85](https://doi.org/10.3847/1538-4357/aada85)
- . 2018b, *ApJ*, 866, 2, doi: [10.3847/1538-4357/aada7c](https://doi.org/10.3847/1538-4357/aada7c)